Phase Separation and Crystallization in Undercooled Pd-Si Melts

Ph. D.

Lee Ka-lun

The Chinese University of Hong Kong

1996

Phase Separation and Crystallization in Undercooled Pd-Si Melts

過冷鈀-硅熔体的相分离及結晶

by

Lee Ka-lun

(李家麟)

A Thesis Submitted in Partial Fulfillment

of the Requirements for the Degree of

Doctor of Philosophy in Physics

The Chinese University of Hong Kong

June 1996

Acknowledgments

I would like to express my deep gratitude to my advisor Dr. Kui hin-wing for his excellent guidance and constant encouragement. I have learnt so much from him.

I would like to thank Dr. Xiao jian-zhong and Mr. Yang hua for their invaluable support and advices.

I should also thank Mr. Yuen cheong-wing, Mr. Chua lai-fei and Mr. Leung kwok-kuen for their kind support and useful discussions.

Finally, I deeply thank my wife.

Abstract

$Pd_{80}Si_{20}$ melts purified by glass fluxing technique could be undercooled (at a rate of 8 K/min) substantially below the liquidus T_l and crystallized at different undercoolings ΔT's, defined by $\Delta T = T_l - T_k$ where T_k is the kinetic crystallization temperature. The microstructures of these undercooled specimens exhibit phase separation in the undercooled liquid state.

Three undercooling regimes can be identified according to the microstructures of the specimens. For $\Delta T \leq 190$ K, the microstructure is typically large dendritic precipitates of Pd_3Si with eutectic background of Pd_5Si and Pd. For $220 \text{ K} \geq \Delta T \geq 190$ K, spherical grains of Pd_3Si (~ 30 μm) are found in a matrix of Pd_5Si. Pd precipitates are scattering all over the specimen. For $\Delta T \geq 220$ K, a fine (~ 1 μm) connected structure with two sub-networks of Pd_3Si and Pd_5Si was located. Small Pd precipitates are found inside and at the edges of the Pd_3Si sub-network. There is a sharp change in dimensions of the microstructures across $\Delta T = 220$ K. Since the crystalline phases in the intermediate and largest undercooling regimes are the same and the cooling rate is slow, grain refinement is not possible. Therefore, the connectivity in microstructure cannot be brought about by coarsening. It is concluded that phase separation has ocurred in the undercooled liquid state. Accordingly, the largest undercooling regime corresponds to liquid spinodal decomposition and the intermediate undercooling regime corresponds to liquid phase separation by nucleation and growth.

The crystallization of the spinodal decomposed melts of $Pd_{80}Si_{20}$ was then studied in detials. Since spinodal decomposition is a spontaneous reaction, the melts undercooled more than 220 K always crystallize to form a fine connected structure of Pd_3Si and Pd_5Si. The microstructures indicate that the crystallization of the Pd_3Si sub-network precedes and triggers the crystallization of Pd_5Si sub-network. After solidification, the original isotropic spinodal morphology of the melt is basically preserved in the crystalline state but partially distorted by the aligning effect due to volume contraction and the coarsening effect due to the latent heat released during crystallization.

The phenomenon of liquid phase separation was also observed in the undercooled melts of $Pd_{40.5}Ni_{40.5}P_{19}$ alloy. The liquid state phase separation by nucleation and growth takes place for $\Delta T \leq 60$ K while that by spinodal decomposition occurs for $\Delta T \geq 100$ K. For $60 \leq \Delta T \leq 100$ K, microstructures indicate that it is the no-theory regime. For $\Delta T \leq 60$ K, two dendrites systems are found in the microstructure, which are $Pd_{30}Ni_{45}P_{25}$ dendrites surrounded by a ternary eutectic and $Pd_{40}Ni_{60}$ dendrites surrounded by a binary eutectic. For $\Delta T \geq 100$ K, during liquid state spinodal decomposition, a system consists of two liquid networks appears initially, which is replaced subsequently by a system of three liquid networks. After crystallization, it gives a fine (~ 0.2 μm) network structure of three interconnected phases with compositions $Pd_{35}Ni_{40}P_{25}$, $Pd_{40}Ni_{60}$ and $Pd_{70}Ni_8P_{22}$.

Table of Contents

Chapter One

Introduction

1.1 Phase Separation in Glass-Forming Alloys

1.1.1 Metallic Glass

An amorphous or non-crystalline solid is a rigid material whose structure lacks crystalline periodicity, that is, the pattern of its constituent atoms or molecules does not repeat periodically in three dimensions. Materials of every bonding type can be quenched into amorphous state; some typical examples are the covalent bonded SiO_2, the metallic bonded $Au_{80}Si_{20}$ and the polymeric bonded polystyrene. There are many different techniques that can be used to produce amorphous materials, for example, melt-quenching, vapour deposition, sputtering and etc. Glass is a major type of amorphous solid which is prepared by melt-quenching method. Since our research mainly concerns with metallic glass, we shall briefly introduce the concepts about glass formation in the following.

When a liquid is undercooled below its melting temperature T_l, it enters a state of metastable equilibrium. If the thermodynamic barrier to crystallization can be overcome, the liquid will crystallize. Otherwise, it remains in metastable equilibrium below T_l and continues to contract at a high rate. At lower temperatures, the atomic mobility of the liquid decreases while its viscosity η increases until it becomes a solid at $\eta \geq 10^{15}$ poise ($\eta = 10^{15}$ poise is the criteria distinguishing solid and liquid). The solid as formed is a 'frozen liquid', called glass, which lacks long range order. This kind of solidification by continuously hardening a liquid is called glass formation. The corresponding temperature at which $\eta = 10^{15}$ poise is the glass transition temperature, T_g. Glass transition is generally accompanied with abrupt changes in thermal expansion coeficient and specific heat capacity.

The crucial requirement in forming a glass is to suppress crystallization during quenching. The usual method to achieve it is to increase the quenching rate. The ease of glass formation of a material is indicated by the critical cooling rate required to quench it into a glass. In principle, any material can be quenched into a glass at a fast enough rate. For a pure metal, the critical rate is estimated to be about 10^{12} K/s. In alloys, the critical cooling rate is reduced to about 10^{6} K/s. There are many factors that affect the glass-forming-ability of alloys. One of the most important rules is to look for deep eutectic systems. The favourable factor is that the melting point near the eutectic composition is very deep and so the metastable liquid is less undercooled at T_g, thereby reducing the possibility of crystallization. Indeed, Marcus and Turnbull [1] proposed that the scaling parameter for glass-forming-ability is T_g / T_l.

1.1.2 Phase Separation in Metallic Glasses

In most of the metallic glasses formed by melt-quenching, inhomogeneities are found only down to a scale of a few Å. Therefore, most metallic glasses are regarded as homogeneous with short range order, but lack long range order. On the other hand, phase separation in the glass state or amorphous phase separation has been reported in a number of melt-quenched metallic glasses on annealing near T_g, for example, in $Pd_{78}Au_6Si_{16}$ [2], $Cu_{59}Zr_{41}$ [3] and $La_{55}Al_{25}Ni_{20}$ [4]. Indeed, in $Ti_{24}Zr_{36}Be_{40}$ [5] and $Pb_{22.5}Sb_{22.5}Au_{55}$ [6], the as quenched specimens display two interconnected amorphous phases.

All the alloys mentioned above are eutectic systems, which favour glass formation. An eutectic system, by definition, is a system in which like species tend to cluster together while unlike kinds are less attracted to each other. The clustering

effect in the solid state of a binary eutectic system results in partial miscibility between two solid phases in the phase diagram. For the liquid state of the same system, we would expect the same clustering effect if the character of the bondings is qualitatively the same in both the solid and liquid state. However, the much larger entropic contribution in the free energy of the liquid state always forces complete mixing of the contituent species in the liquid at high temperatures. It is only at very low temperatures that the entropic contribution diminishes and liquid immiscibility appear (because the entropic contribution in the free energy is weighed by temperature : G = H - TS). Hence, a liquid miscibility gap should lie in the undercooling regime in an eutectic system, near the eutectic composition.

Kinetically, phase separation still requires sufficient time and atomic mobility to process. In the preparation of metallic glass by melt-quenching method, the cooling rate is probably too fast for phase separation to happen. Hence in most cases we obtain homogeneous glasses. Then if we anneal the homogeneous glasses around T_g, they become kinetically relaxed and phase separation may occur. These account for the phenomenon of phase separation observed in the metallic glasses in Ref. [2-6].

1.1.3 Phase Separation in the Undercooled Melts of Glass-Forming Alloys

Recently, Busch [7] even found evidence of decomposition in the undercooled melt during the formation of the metallic glass $Zr_{41.2}Ti_{13.8}Cu_{12.5}Ni_{10.0}Be_{22.5}$. Indeed, we suggest that there exists a metastable liquid miscibility gap in all glass-forming eutectic systems at low enough temperatures. To study this miscibility gap, the method of rapid melt-quenching used in the preparation of metallic glass may be too fast for the completion of the liquid phase separation in the undercooled state, for at a cooling rate

of 10^6 K/s, a melt has been exposed to the undercooling regime for only ~10^{-3} s. To attain high undercoolings of molten metals at a slower cooling rate, a fluxing technique is most appropriate. It was demonstrated repeatedly that by fluxing molten metals or alloys with molten anhydrous boron oxide, they can be undercooled substantially below their melting points or liquidus. In this way, $Pd_{40}Ni_{40}P_{20}$ can be undercooled to its glassy state with a cooling rate of 0.75 Ks^{-1} [8] and molten Ge can be undercooled by 342 K below its melting point with a cooling rate of 6 $Kmin^{-1}$ [9]. In this thesis, this fluxing technique was applied to molten $Pd_{80}Si_{20}$ and $Pd_{40.5}Ni_{40.5}P_{19}$ alloys to achieve high undercoolings at a slow cooling rate in order to determine the transition temperatures of the metastable liquid miscibility gap. $Pd_{80}Si_{20}$ and $Pd_{40.5}Ni_{40.5}P_{19}$ are chosen for they are eutectic alloys and evidences of phase separation near T_g have been reported in both cases [2,10].

1.2 Theory of Phase Separation

1.2.1 Thermodynamics of Phase Separation

In this section, we introduce the theory of phase separation in the systems whose free energy plotted against composition can be described by a single smooth curve, for example, the systems of alloy in the liquid state.

Phase separation is originated from a region of negative curvature in the free energy diagram plotted against composition. This can happen only in systems with a positive enthalpy of mixing. Consider the simpler case of a binary system with a positive enthalply of mixing. The free energy of the binary solution of atoms A and atoms B can be written as

$$G = G_A C_A + G_B C_B + \Delta G_m = G_o + \Delta G_m \quad (1)$$

where C_A and C_B are the atomic fractions of the atoms A and B, G_0 is the sum of the free energy of pure A and pure B and ΔG_m is the free energy contributed by mixing A and B. ΔG_m is composed of

$$\Delta G_m = \Delta H_m - T\Delta S_m \quad (2)$$

where ΔH_m is the enthalpy of mixing and ΔS_m is the entropy of mixing. At high temperatures, the entropic contribution forces complete mixing of the constituent atoms and a homogeneous phase is expected. The corresponding free energy curve is shown in Fig. 1. However, when the temperature is low enough, then the positive enthalpy of mixing dominates, resulting in phase separation. The free energy of an originally homogeneous phase α would be lowered by δG if it decomposes into α_a and α_b as shown in Fig. 2. If the concentration of the initial homogeneous phase lies within region I bounded by the points of inflexion as shown in Fig. 3, a local fluctuation in concentration would lower the free energy by δG. Therefore, a homogeneous phase in region I would spontaneously decompose (spinodal decomposition) by diffusion into the two phases α_a and α_b. On the contrary, a homogeneous phase in region II is locally stable as a fluctuation in concentration would raise its free energy. Therefore, in region II_a, nucleation and growth of a second phase α_b is required to bring about phase separation (the situation is the same for II_b). The two final phase separated phases are also α_a and α_b.

This kind of free energy curves for different temperatures combine to form a miscibility gap in the phase diagram as shown in Fig. 4. Therefore, when a homogeneous system is cooled down into region II in the phase diagram, it would

phase separate by nucleation and growth; if a homogeneous system is quenched into region I, it would undergo spinodal decomposition. In both cases, the compositions of the two final phase separated phases are marked by the miscibility gap at that temperature.

1.2.2 Phase Separation by Nucleation and Growth

An initially homogeneous system lying in region II in Fig. 3 would phase separate to lower its free energy by nucleation and growth. The process of nucleation and growth is the formation of a small nucleus of a new phase in the mother phase (nucleation) and the subsequent growth of the nucleus by advancement of the newly formed interface (growth). For instance, if the initial system of composition α_o lies in region II_a, it would not spontaneously decompose into phase α_a and α_b because of the energy barrier. The phase separation would begin by forming small nuclei of phase α_b in the mother phase α_o. Then the nuclei would grow larger and larger by diffusion through the interface while the composition of the mother phase α_o would approach that of phase α_a. This ends up with a mixture of the two phases α_a and α_b with their ratio determined by lever rule. Consequently, the microstructure of the resulting phase separated specimen would consist of 'islands' of phase α_b scattering in a 'sea' of phase α_a . Hence, for liquid phase separation by nucleation and growth, we would expect droplets of phase α_b distributing in a sea of phase α_a.

The process of nucleation and growth requires activation energy for creating the interfaces between the nuclei and the mother phase. Presence of impurities will lower this activation energy. Hence, in our study of liquid phase separation, if the

specimen is clean enough, the undercooled liquid would bypass the liquid phase separation by nucleation and growth and directly reach the liquid spinodal region.

1.2.3 Cahn's Theory of Spinodal Decomposition

The development of the composition profile during phase separation is shown schematically in Fig. 5a for the case of nucleation and growth and Fig. 5b for the case of spinodal decomposition. Cahn [11, 12] had made a successful derivation of the spinodal decomposition which results in a composition evolution as shown in Fig. 5b. In the following paragraghs, Cahn's derivation, described in Hilliard's article [13], will be introduced in detail. However, the effect of elastic strains is ignored for we are dealing with liquids. For mathematical simplicity, the treatment is restricted to one dimensional problem.

In the binary system of atoms A and B, the fluxes of atoms J_A and J_B are proportional to the gradient in chemical potentials,

$$\begin{aligned} J_A &= -N_V (1-C) V_A \frac{\partial \mu_A}{\partial x}, \\ J_B &= -N_V C V_B \frac{\partial \mu_B}{\partial x}, \end{aligned} \tag{3}$$

where V's are the velocities of the atoms under a unit potential gradient, μ's are the chemical potential per atom, N_V is the number of atoms per unit volume and C is the atomic fraction of B. We can always choose a moving reference plane (Matano interface) at which the total net flux is zero. In such a frame the flux of atoms B is

$$J = J_B - C(J_A + J_B) = -N_V C\left[V_B\left(\frac{\partial \mu_B}{\partial x}\right) - V_A\left(\frac{\partial \mu_A}{\partial x}\right)\right]$$

$$= -N_V C(1-C)\left\{[(1-C)V_B + CV_A]\left[\left(\frac{\partial \mu_B}{\partial x}\right) - \left(\frac{\partial \mu_A}{\partial x}\right)\right] + (V_B - V_A)\left[C\left(\frac{\partial \mu_B}{\partial x}\right) + (1-C)\left(\frac{\partial \mu_A}{\partial x}\right)\right]\right\}$$

Assuming Gibbs-Duhem equation applies, that is,

$$(1-C)\partial\mu_A + C\partial\mu_B = 0 . \quad (4)$$

Therefore the second term in the last expression of J is zero, giving

$$J = -MN_V \frac{\partial}{\partial x}(\mu_B - \mu_A) \quad (5)$$

where M is the mobility defined by

$$M = C(1-C)[(1-C)V_B + CV_A] . \quad (6)$$

For a homogeneous system,

$$N_V(\mu_B - \mu_A) = \frac{\partial g}{\partial C} \quad (7)$$

where g is the free energy of the system per unit volume. However, for the decomposing systems that we are interested in, the atoms will be aware of the compositional inhomogeneity of their enviroment. This leads to a modification in the chemical potential:

$$N_V(\mu_B - \mu_A) = \frac{\partial g}{\partial C} - 2K\frac{\partial^2 C}{\partial x^2} . \quad (8)$$

The addition of the last term can be explained as follows. For a region where the composition of B has a positive curvature, $\frac{\partial^2 C}{\partial x^2}$, a B atom will have more B atoms in its surroundings than the homogeneous case. For systems with positive interaction energy between unlike atoms (positive enthalpy of mixing), this will give a lower chemical potential of B than the homogeneous case. Therefore, it is necessary to deduct from (μ_B - μ_A) a term proportional to the curvature $\frac{\partial^2 C}{\partial x^2}$ when the composition

of the system deviates from homogeneity. In fact the deviation from homogeneity can be regarded as the formation of a diffuse interface between two phases. Hence, the term $\frac{\partial^2 C}{\partial x^2}$ can be associated with the excess free energy contributed by such an interface. Then, substituting the last equation into the equation of J, we get

$$J = -M\frac{\partial}{\partial x}\left(\frac{\partial g}{\partial C} - 2K\frac{\partial^2 C}{\partial x^2}\right) = -M\frac{\partial}{\partial x}\left(\frac{\partial g}{\partial C}\right) + 2KM\frac{\partial^3 C}{\partial x^3}$$
$$= -M\frac{\partial^2 g}{\partial C^2}\frac{\partial C}{\partial x} + 2MK\frac{\partial^3 C}{\partial x^3} . \qquad (9)$$

The conservation equation becomes

$$\frac{\partial C}{\partial t} = -\frac{1}{N_V}\frac{\partial J}{\partial x} = \frac{M}{N_V}\left(g''\frac{\partial^2 C}{\partial x^2} - 2K\frac{\partial^4 C}{\partial x^4}\right) . \qquad (10)$$

This equation has a sinusoidal wave solution:

$$C - C_o = e^{R(\beta)t}\cos\beta x \qquad (11)$$

where the amplification factor

$$R(\beta) = -\frac{M}{N_V}\beta^2(g''+2K\beta^2). \qquad (12)$$

When the composition of the system lies within the points of inflexion of the free energy curve as shown in Fig. 3, g'' is negative. For negative g'' , the value of R(β) is plotted in Fig. 6. It has a maximum value at β_m. Since the maximum is very steep and it occurs in the exponential amplitude of C - C_0, the growth of the sine wave solution with wavelength corresponding to β_m would be selectively amplified and all other wavelengths can be ignored. Therefore, the evolution of the concentration can be described by

$$C - C_o = e^{R(\beta_m)t}\cos\beta_m x \qquad (13)$$

where

$$\beta_m = \frac{1}{2}\left(-\frac{g''}{K}\right)^{1/2}. \qquad (14)$$

The time dependent behavior can be pictured by Fig. 5b.

In three dimensional space, Cahn [14] had simulated the morphology of the spinodal decomposition of an isotropic material for $C_0 = 0.5$ by the superposition of 100 random (in direction and phase) sine waves with wavelength λ. The cross-section of the resulting structure is shown in Fig. 7. It is clear that the connectivity of the two phases is the characteristic of an isotropic spinodal structure with the two phases having approximately the same volume fractions. (However, interconnectivity cannot be regarded as a sufficient proof of spinodal decomposition because Seward, Uhlmann and Turnbull [15] have shown that discrete particles can become interconnected by coalescence.)

Cahn's theory is a successful theory for spinodal decomposition. In case of solid state, Cahn introduced a term of elastic strain and estimated the correct order of the wavelength (~100 Å) of the spinodal structure. The spinodal morphology in Fig. 7 is also practically observed in isotropic systems. Therefore, in our study of phase separation in metallic liquid, the spatial morphology in Fig. 7 together with the composition evolution in Fig. 5b can be used as the guidelines for describing the spinodal decomposing process.

1.3 Experimental Method to Achieve High Undercooling

In order to study the metastable liquid phase separation in glass-forming eutectic alloy, it is desirable to undercool the alloy melt slowly to way below its T_l. However, due to the presence of impurities, most often it solidifies immediately below T_l. The crystallization begins with the formation of very small solid particles and then they grow larger and larger until consuming all the liquid (the process of nucleation and growth). Normally, the wall of the liquid container and solid impurity particles in the liquid catalyse the crystallization at undercoolings of a few degree K below T_l. In order to achieve high undercoolings at slow cooling rates, we employ the boron oxide fluxing technique [16] to remove the impurities and hence suppress the heterogeneous nucleation. In this section, we shall describe this method used to undercool the melt of Pd-Si alloy.

Pd-Si ingot of ~ 1g was prepared from pure elemental Pd and Si ingots. After weighing in right proportion, they were put into a clean fused silica tube and alloying was brought about by radio frequency (rf) induction heating.

In the experiment, an as prepared specimen was put into a clean fused silica tube together with pieces of anhydrous B_2O_3 ingots. The fused silica tube had been cleaned beforehand by filling it with HF and HNO_3 in a ratio of 2:3 for 10 min to remove the impurities on the inner surface. The specimen and the anhydrous B_2O_3 were melted inside the tube by a torch under a vacuum of ~ 10^{-3} Torr. The system was then heated up to ~ 1300 K to facilitate the removal of impurities from the molten specimen. At such a high temperature, reactive metals such as Mg, Al and Ca etc. that appear as impurities would eventually be oxidized since they have strong affinity for oxygen. All these oxides would finally be segregated to the specimen-boron oxide interface due to gravity segregation and then dissolved by the boron oxide. Other

impurities can be deactivated by dissociating in the molten specimen at such a high temperature.

After the heat treatment, the whole system was transferred into a Transtemp furnace. The schematic diagram of the set up is shown in Fig. 8. The Transtemp furnace consists of two concentric fused silica tubes. A heating coil is wound around the inner tube while the outer one is plated with a thin layer of gold on its inner surface. Since the gold layer is very thin, any visible change on the specimen surface can be observed directly. The temperature of the specimen was recorded by a thermocouple which was sheathed by a smaller clean fused silica tube and touched the specimen. The thermocouple was connected to an X-T recorder. Initially, the furnace was set at a temperature above the liquidus of the specimen. We waited for 15 min for the establishment of thermal equilibrium between the molten specimen and the furnace. Then the furnace was allowed to cool down at a rate of 8 K/min. As soon as the thermocouple recorded the peaks due to the release of heat of crystallization, the fused silica tube holding the specimen was taken out of the furnace and was allowed to cool down in air. By this method, a $Pd_{80}Si_{20}$ alloy melt can be undercooled by as much as 300 K below T_l at the cooling rate of 8 K/min.

The specimens crystallized at different undercoolings were cut, polished and etched in an etchant of $HCl:HNO_3:H_2O$ = 5:1:3.The microstructures were then studied by optical microscopy, electron micrscopy and EDX analysis.

References

1. M.A. Marcus and D. Turnbull, Mater. Sci. Eng. 23, 211 (1976).
2. H.S. Chen and D. Turnbull, Acta Metall. 17, 1021 (1969).
3. D. Deng and A.S. Argon, Acta Metall. 34, 2011 (1986).
4. H. Okumura, A. Inoue and T. Masumoto, Acta Metall. 41, 915 (1993).
5. L.E. Tanner and R. Ray, Scr. Metall. 14, 657 (1980).
6. C.O. Kim and W.L. Johnson, Phys. Rev. B 23, 143 (1981).
7. R. Busch, S. Schneider, A. Peker and W.L. Johnson, Appl. Phys. Lett. 67, 1544 (1995).
8. H.W. Kui and D. Turnbull, Appl. Phys. Lett. 45, 615 (1984).
9. C.F. Lau and H.W. Kui, J. Appl. Phys. 67, 3181 (1990).
10. H.S. Chen, Mater. Sci. Eng. 23, 151 (1976).
11. J.W. Cahn, Acta Metall. 9, 795 (1961).
12. J.W. Cahn, Acta Metall. 10, 179 (1962).
13. J.E. Hilliard, in 'H.I. Aaronson (Ed.) :Phase Transformation', 497 (ASM, 1970).
14. J.W. Cahn, J. Chem. Phys. 42, 93 (1965).
15. T.P. Seward III, D.R. Uhlmann and D. Turnbull, J. Am. Ceram. Soc. 51, 634 (1968).
16. J.L. Walker, in 'B. Chalmers (Ed.): Principle of Solidification', 114 and 122 (Wiley, 1964).

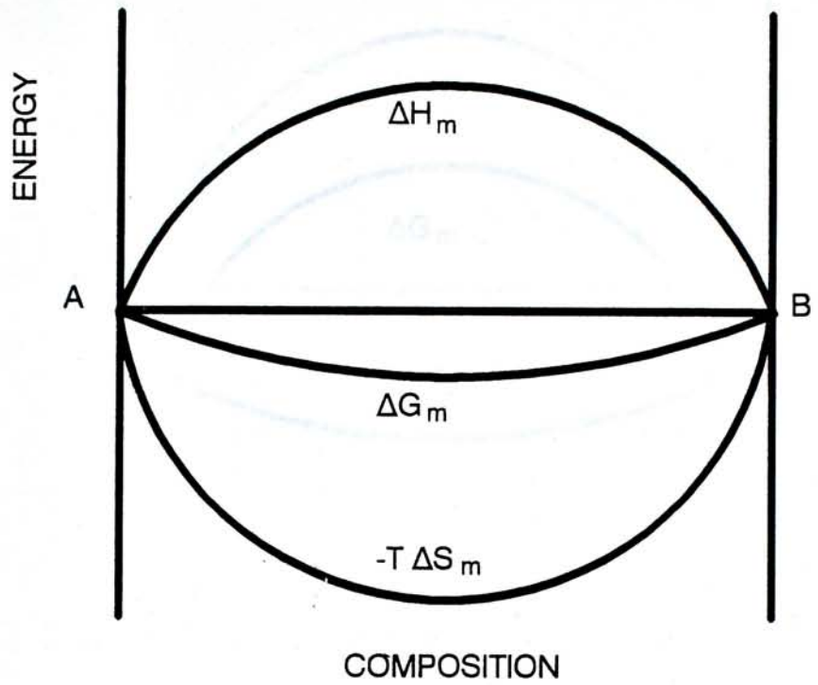

Fig. 1a ΔH_m, $-T\Delta S_m$ and ΔG_m at a high temperature.

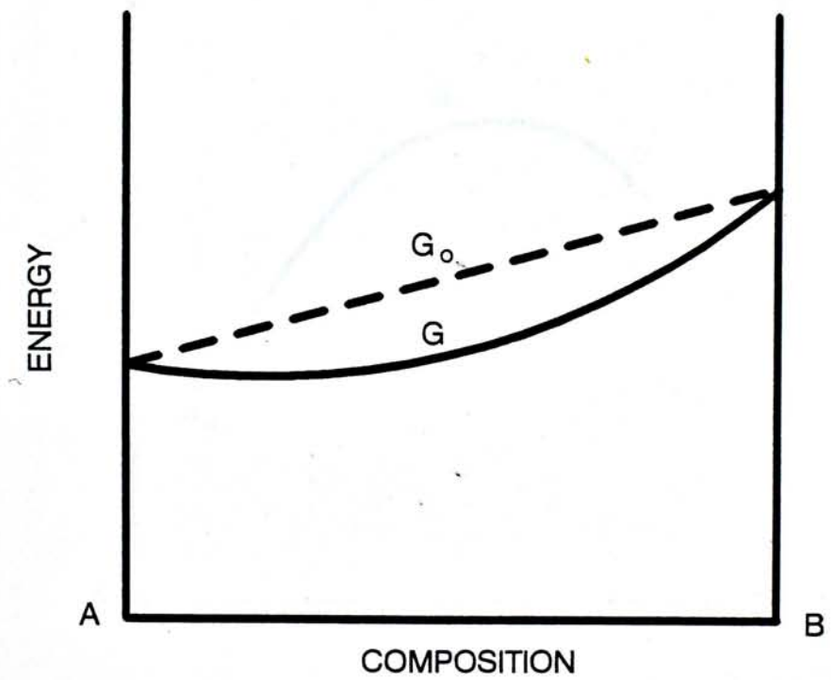

Fig. 1b Resulting free energy curve of Fig. 1a.

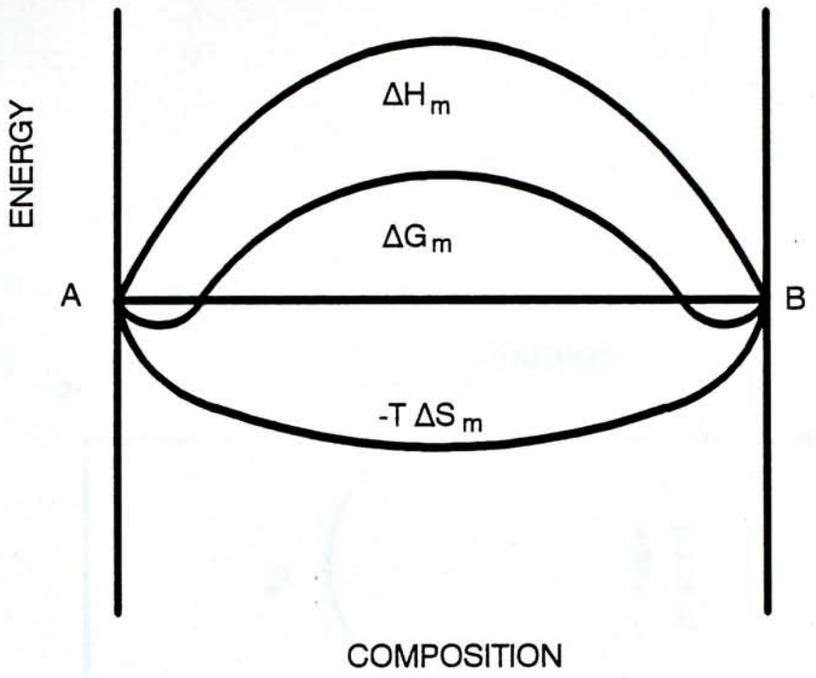

Fig. 2a ΔH_m , $-T\Delta S_m$ and ΔG_m at a low enough temperature.

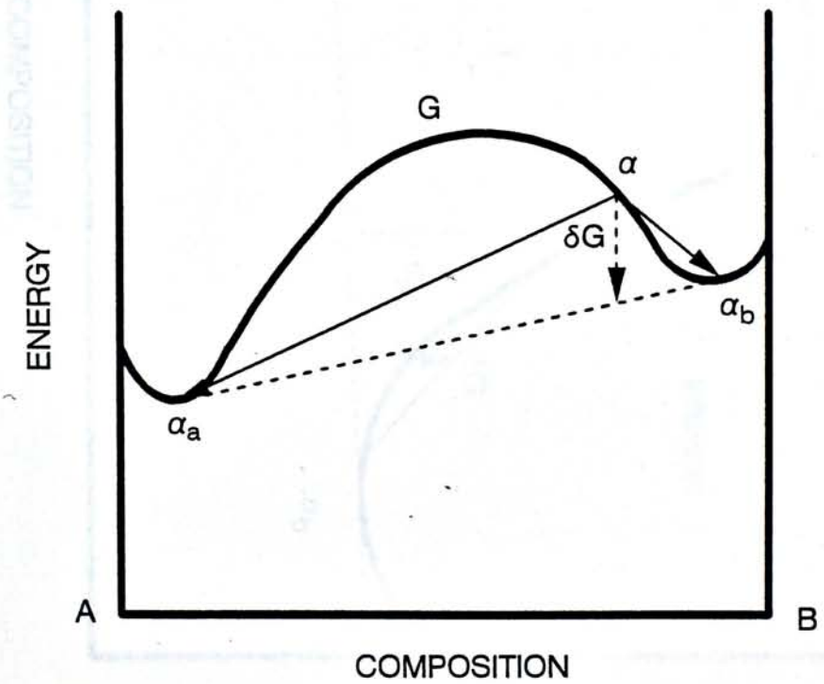

Fig. 2b Resulting free energy curve of Fig. 2a showing phase separation.

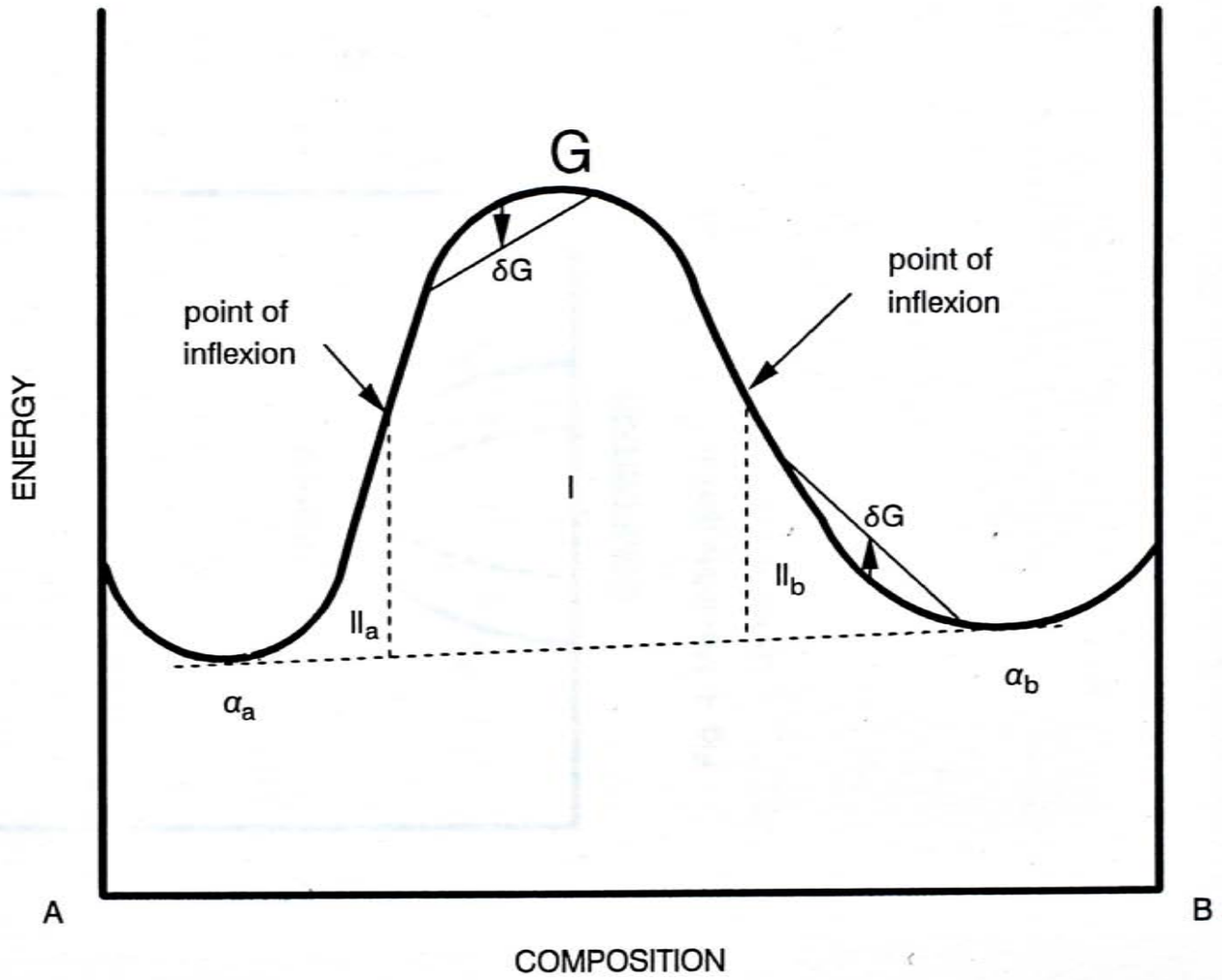

Fig. 3 Region I: region of spinodal decomposition;
region II: region of phase separation by nucleation and growth.

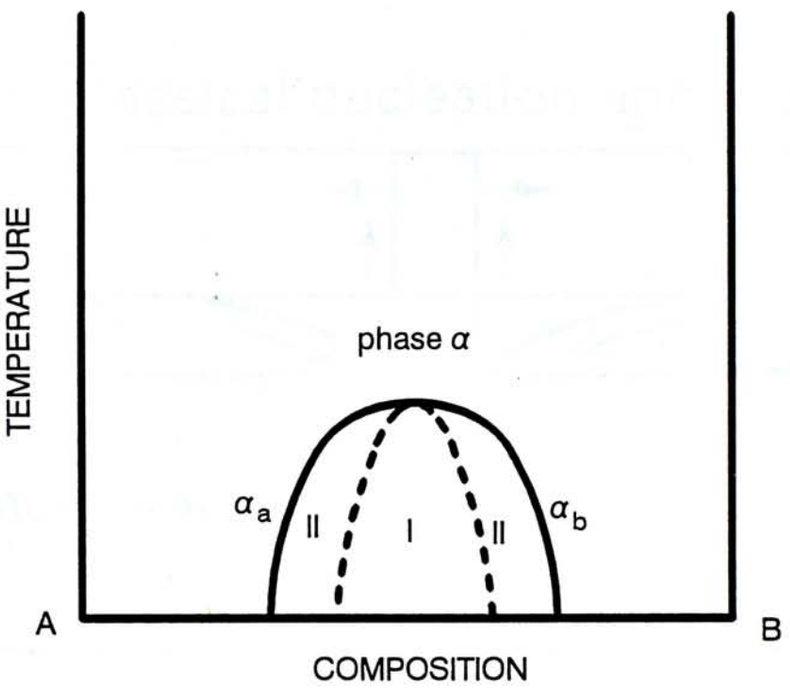

Fig. 4 Miscibility gap and spinodal curve in the phase diagram.

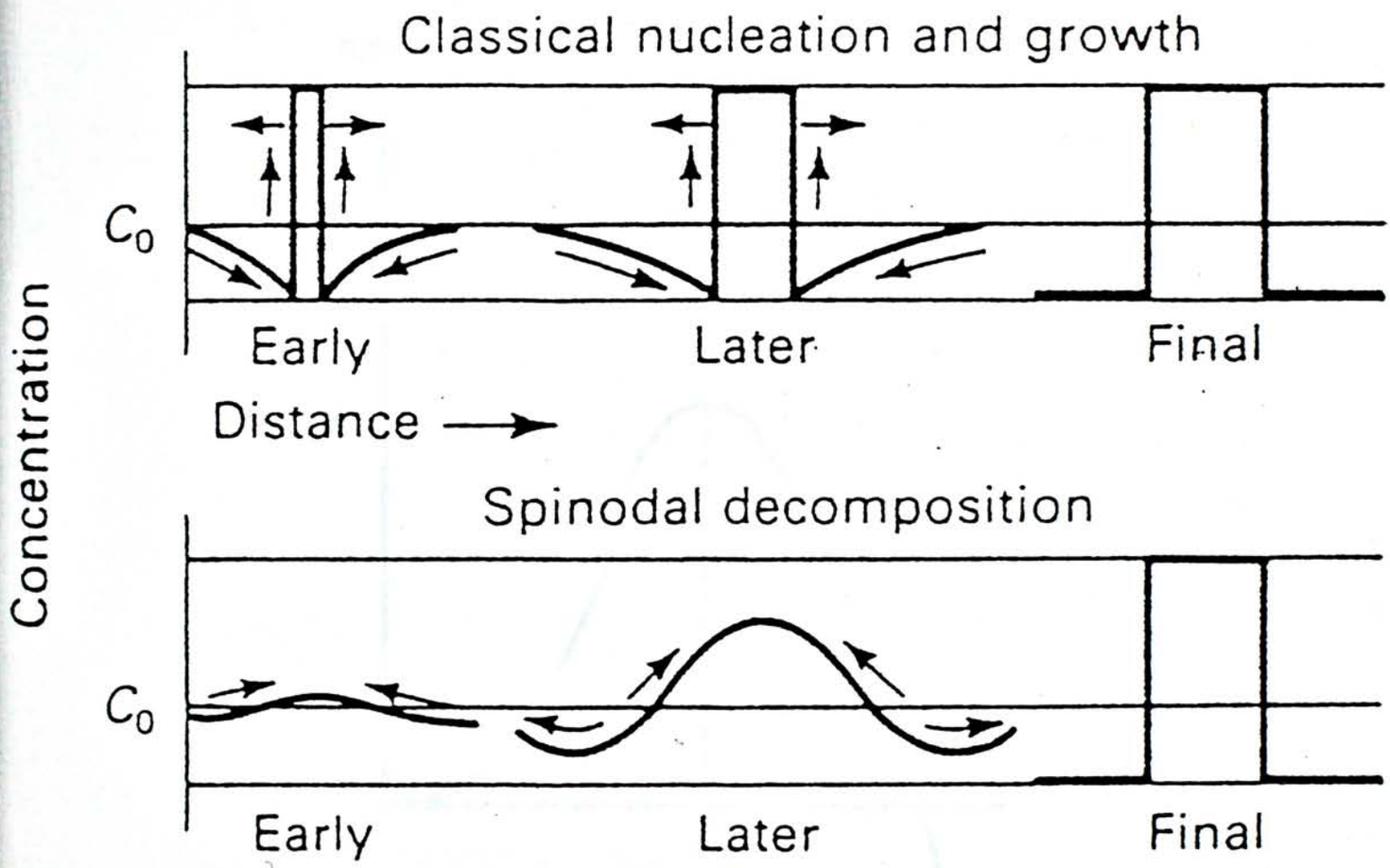

Fig. 5a Upper : Composition evolution for phase separation by nucleation and growth.

Fig. 5b Lower : by spinodal decomposition.

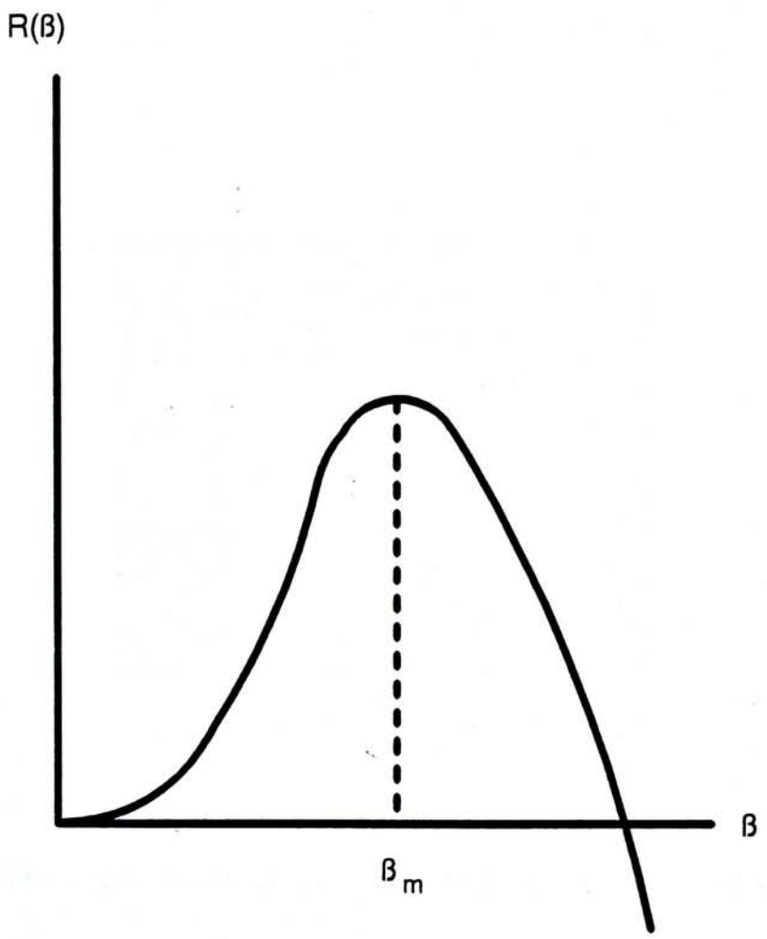

Fig. 6 Amplification factor R(β).

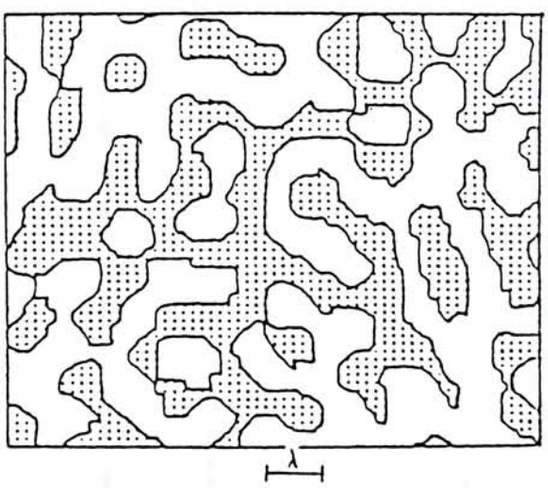

Fig. 7 Cross-section of isotropic spinodal structure with $C_0 = 0.5$. The composition of the shaded region is greater than C_0.

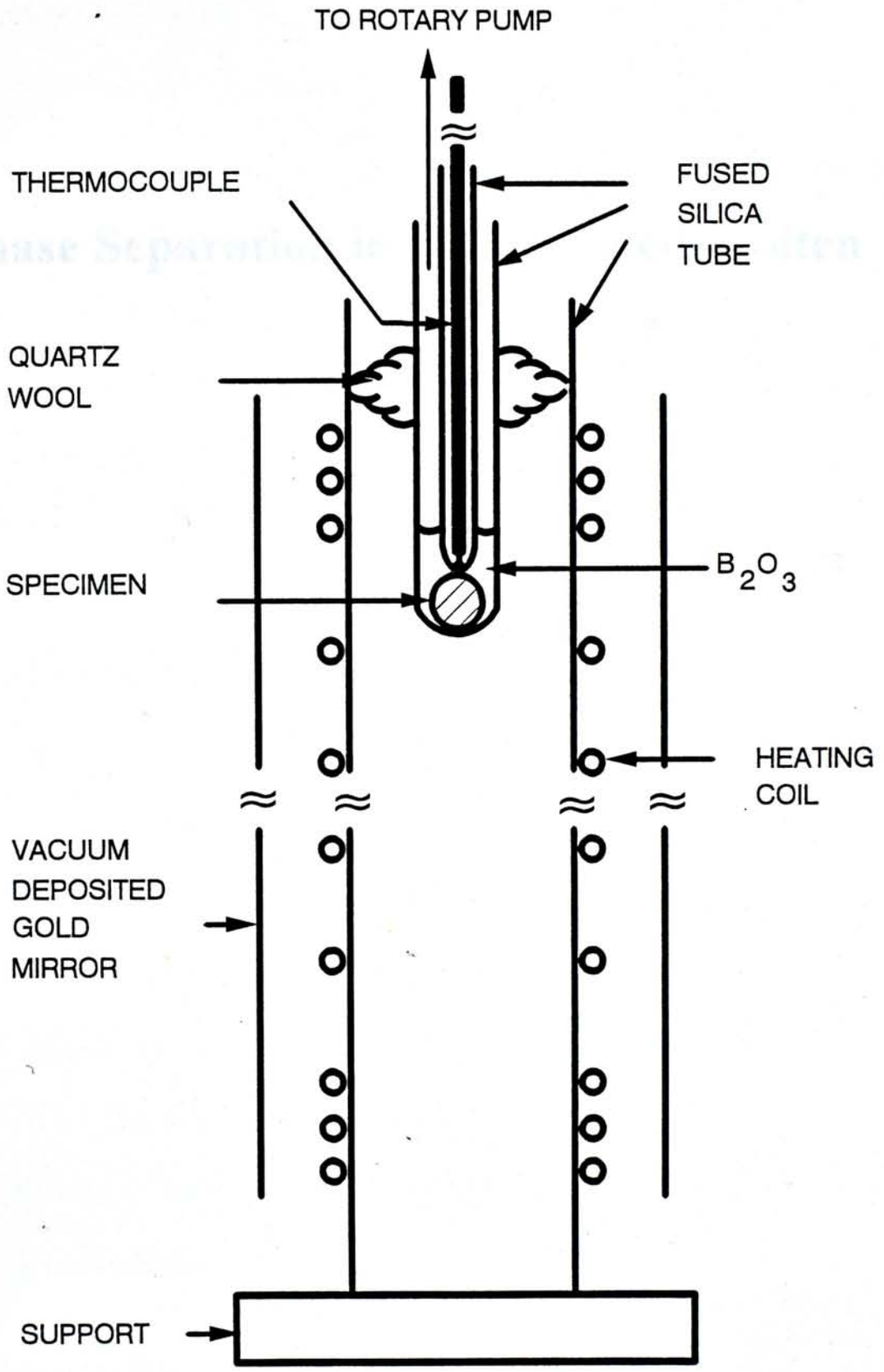

Fig. 8 Schematic diagram of apparatus used to record the temperature profile of the molten specimen.

Chapter Two

Phase Separation in Undercooled Molten $Pd_{80}Si_{20}$

(submitted to Acta Metall.)

Phase separation in undercooled molten $Pd_{80}Si_{20}$

K.L. Lee and H.W. Kui

Department of Physics, The Chinese University of Hong Kong

Shatin, N.T., Hong Kong

Abstract

Three different kinds of morphology were found in undercooled $Pd_{80}Si_{20}$ and they appear at different undercooling regimes. In the least undercooling regime, $\Delta T \leq 190$ K, the microstructures are typically dendritic precipitation with eutectic background. In the intermediate undercooling regime, spherical morphologies which arise from nucleation and growth mode is found. There are Pd precipitates scattered all over the undercooled specimen. In the largest undercooling regime, a connected structure composed of two sub-networks was located. There is a sharp decrease in the dimensions of microstructures as one moves from the intermediate to the largest undercooling regime. Since the crystalline phases in the intermediate and largest undercooling regimes are the same and the cooling rate is slow, grain refinement is not possible. Therefore the connectivity in microstructure cannot be brought about by coarsening. It is concluded that phase separation has taken place in undercooled $Pd_{80}Si_{20}$. Furthermore, according to the crystallization behavior, the phase separation has occurred in the undercooled liquid state.

Introduction

By definition, the like species in a eutectic alloy attract each other while the unlike kinds repel each other. The free energy of the solid phase of the eutectic alloy can be described either by different free energy curves (compound formation) or by a single free energy curve with a hump in between (without compound). The behavior in the latter is termed partial miscibility in the solid state.

For the same eutectic alloy in the liquid state, if the magnitude of the interactions between the like and unlike species remains qualitatively the same, it is plausible to assume that the free energy curve is also described by a smooth curve with a hump in between, same as its crystalline counterpart, when the temperature is low enough. Indeed, due to the relaxed condition on meeting the long range order in the liquid state, it is very possible that even if there are independent free energy curves in the solid state, the free energy curve of the liquid state can still be described by a single smooth curve. Again, at high temperatures, due to the entropic contribution, the molten alloy is a homogeneous liquid. On the other hand, at low temperatures, partial miscibility is expected for like species which prefer to stay together.

The phase separation can also be understood through the Gibbs free energy G defined as G = H - TS where H is the enthalpy, T is the temperature of the system and S is the entropy. At high temperatures, the entropic contribution dominates and complete mixing of the constituent atoms is expected. However, at low temperature, the entropic contribution S is too insignificant to bring about complete mixing of the different atoms. As a result, H dominates, favoring the clustering of one kind of the constituent atoms or phase separation.

Compared with its crystalline counterpart, a liquid has a larger configurational entropy but smaller enthalpy. Therefore, considering the Gibbs free energy $G = H - TS$, the critical temperature T_c of the liquid miscibility gap may be so low that the melt has to be undercooled to way below its liquidus T_l in order to uncover the phase separation reactions. Experience indicates that upon the cooling of molten eutectic alloys, in most cases solidification prevails immediately below T_l. This, of course, inhibits the manifestation of the liquid state phase separation of the undercooled melt.

Experience [1, 2] indicates that deep eutectic alloys with composition near the eutectic composition are good glass formers. In metallic glass formation by conventional rapid quenching methods, e.g. splat quenching and melt spinning, a melt is rapidly quenched from above its liquidus, bypassing crystallization, to below the glass transition temperature T_g. Therefore, metallic glass is a rigid undercooled liquid with a viscosity larger than $\sim 10^{15}$ poise (relaxed state) [3]. The estimated cooling rate achieved in these conventional quenching methods is $\sim 1 \times 10^6$ K s^{-1} [4]. Therefore, during glass formation by conventional rapid quenching, a molten eutectic alloy has been exposed to the undercooling regime for a period of $\sim 1 \times 10^{-3}$ s. Since spinodal decomposition is a spontaneous reaction, if kinetics is allowed and the time spent in the metastable undercooling regime is long enough, the microstructures of an as quenched undercooled specimen should contain information about the liquid decomposition reaction.

Experience indicates that the as prepared glassy metals possess short range order but lack long range order. However, Chen and Turnbull [5], Chou and Turnbull [6], and Chen [7] observed the formation of another amorphous phase (with different

composition) inside the original amorphous matrix when glassy Pd-Cu-Si, Pd-Au-Si and Pd-Ni-P specimens were heated up from below the T_g to slightly above T_g, respectively. Therefore, amorphous phase separation has been observed and demonstrated in metallic glasses. Unfortunately, upon further heating of the glassy specimens, crystallization always interrupts the decomposition, i.e. only the early stage of the decomposition is known. Chou and Turnbull [6] had carried out time-dependent measurement on the composition variation in Pd-Au-Si at the early stage of the transformation by small angle x-ray scattering method and the results are consistent with predictions from spinodal decomposition mechanism. Later, Tanner [8] observed amorphous phase separation in as quenched Zr-Ti-Be by transmission electron microscopy (TEM). Over the years, efforts [9, 10, 11, 12, 13] have been devoted to unravel the mystery of amorphous phase separation.

Since impurities are unavoidable in a bulk alloy melt, the glassy specimen obtained by rapid-quenching of the bulk melt must still contain those impurities. As soon as it is heated up to above the glass transition temperature to become a viscous liquid, if there are quenched-in nuclei, crystal growth would occur quite readily on these nuclei. When quenched-in nuclei are absent, the kinetics above T_g may be rapid enough to allow for heterogeneous nucleation to take place on those heterogeneous impurities. Therefore, the rapid cooling rate used in the preparation of glassy metals is to suppress the heterogeneous nucleation and also homogeneous nucleation from happening. Now spinodal decomposition is a spontaneous reaction. During rapid quenching, it is expected that partial phase separation can still occur. It is interesting to note that in Tanner's experiment, apparently the quenching rate is fast enough to suppress crystallization, leading to glass formation. Meanwhile, it is slow enough for

the phase separation to occur. This experience reflects that in order to get a complete picture of the decomposition reaction in undercooled molten alloys, it is necessary to observe the following conditions. First, the melts have to be undercooled to way below T_l. Therefore, heterogeneous impurities have to be removed from the molten specimens. Second, the undercooled melts must enter a regime where the nucleation frequency for the formation of another liquid phase is appreciable while that of the formation of a solid phase is still negligible. Finally, the composition of the eutectic alloy melt must be inside the miscibility gap. The second condition above can easily be appreciated. In the absence of heterogeneous impurities, the kinetics barrier for a liquid nucleus is smaller than that of a solid nucleus.

It was demonstrated repeatedly that by a fluxing technique [14, 15], undercooled molten metals can be undercooled substantially below T_l, the liquidus for alloys and the thermodynamic melting temperature T_m for pure elemental metals. For instance, by fluxing molten $Pd_{40}Ni_{40}P_{20}$ in molten anhydrous boron oxide, it can be undercooled to its glassy state bypassing crystallization with a cooling rate of 0.75 K s^{-1} [14, 16]. Also, molten Ge [15] can be undercooled by as much as 342 K below its T_m with a cooling rate of 6 K min^{-1}. In this study, we applied the fluxing technique to $Pd_{80}Si_{20}$ in order to undercool it to way below its T_l. It is expected that when the undercooling is large enough, liquid state phase separation would take place in $Pd_{80}Si_{20}$ for it is a eutectic alloy. Another reason that $Pd_{80}Si_{20}$ was chosen as Chou and Turnbull [6] had demonstrated that upon heating a glassy $Pd_{80}Si_{20}$ (with small amount of Au) specimen to slightly above T_g, phase separation occurs.

Experimental

To form the alloy, weighed elemental Pd (99.99% pure) and Si (99.9999% pure) ingots were alloyed by rf induction melting under Ar atmosphere.

To remove water from boron oxide (99.995% pure), it was preheated at ~ 1273 K for 36 h in a Pt crucible contained in an evacuated (to ~ 10^{-3} Torr) fused silica tube. After cooling to room temperature, the anhydrous boron oxide was stored in a vacuum desiccator until use.

The undercooling of molten $Pd_{80}Si_{20}$ was carried out in a Transtemp furnace which consists of two concentric fused silica tubes. A heating coil is wound around the inner tube while the outer one is plated with a thin layer of gold on its inner surface. The Au coating helps to trap the heat generated from the heating coil from radiating away from the furnace so as to provide a uniform temperature environment inside the chamber of the furnace. Since the Au layer is very thin, any visible change on the specimen surface can be observed directly. The Transtemp furnace is connected to a personal computer (PC) which regulates the power into the furnace and hence it can control a pre-arranged rate of cooling or heating inside the chamber of the furnace. The detailed experimental setup can be found in Ref. [15].

In the experiment, a $Pd_{80}Si_{20}$ ingot and anhydrous boron oxide were put in a dry, cleaned fused silica tube (i.d. = 11mm, o.d. = 13 mm). The system was then heated up to 1273 K by a torch. The high temperature oxide-fluxing of molten $Pd_{80}Si_{20}$ by B_2O_3 enhanced the removal of impurities from the molten specimen. Prolonged heat treatment was applied for ~ 4 h. After the heat treatment, the system was transferred to the Transtemp furnace which was preset at 1273 K, above the liquidus of $Pd_{80}Si_{20}$. The schematic diagram of the experimental setup is shown in Fig. 1. To establish thermal

equilibrium, the system was allowed to sit inside the furnace under isothermal condition for 20 min. Afterwards, the PC regulated the power into the furnace to bring the furnace to cool down at a rate of 8 K min^{-1}. As a result, the molten specimen was simultaneously cooled down at a rate of ~ 8 K min^{-1}. The actual temperature of the molten specimen was read by a thermocouple which was sheathed by another fused silica tube (i.d. = 4 mm, o.d. < 5 mm) and inserted directly into the molten specimen. At the completion of crystallizations, the furnace was cooled down to room temperature. The undercooled specimen was then removed from the furnace and its microstructure was studied in detail. The above procedure was applied to many other specimens and a correlation between undercooling defined as $\Delta T = T_l - T_k$ where T_k is the kinetic crystallization temperature and microstructures can be established. The microstructure is analyzed by standard metallography methods and composition measurement is carried out with an EDX detector attached to a scanning electron microscope (SEM).

Results

At small undercoolings (will be defined later), the temperature profile always shows two peaks. As undercooling increases, the peaks get closer to each other and finally at very large undercoolings (again will be defined later), very often there is only one peak though at times two overlapping peaks appear. The maximum undercooling recorded by the continuous cooling method (cooling rate = 8 K min^{-1}) described above is 300 K. Microstructural analysis indicates that based on morphological changes, three undercooling regimes can be distinguished. The temperature range of each regime is based on the position of the first crystallization peak in the temperature profile.

In the least undercooling regime defined as $0 \leq \Delta T \leq 190$ K, a typical temperature profile is shown in Fig. 2. It displays two peaks. The nature of these two peaks is not known. Since the starting material is a molten alloy and the final product is crystalline, it is suspected that both peaks correspond to crystallizations. In order to confirm this supposition, the following experimental procedure had been undertaken: Since the Transtemp furnace is transparent, crystallization process could be observed directly by us. It was found that as a molten specimen was cooled below T_l passing through the first peak, the specimen surface remained shiny as if nothing had happened. Right after the first peak, the continuous cooling mode was modified to isothermal condition and the specimen was subject to mechanical testing. Indeed, mechanical stirring of the undercooled specimen by the fused silica tube which sheathed the thermocouple was still possible indicating that the undercooled specimen was at least still partially molten. On the other hand, during stirring, tiny solid particles were brought onto the surface of the specimen confirming that the physical state of the specimen after the first peak is a liquid in which small crystallites are dispersed. This physical state transforms to a complete solid on reaching the second peak for the specimen surface roughened and the fused silica tube could no longer penetrate into the specimen. It is therefore concluded that the two peaks shown in Fig. 2 are crystallization peaks.

In most continuous cooling experiments, after the appearance of the first crystallization peak, the second peak occurred at an undercooling of ~ 230 K. In all cases, the onset of the second peak never occurred below $\Delta T > 240$ K. However, after the appearance of the first crystallization peak, the second peak could be brought about by stirring vigorously the liquid-crystallites mixture with the fused silica tube that

was used to sheathe the thermocouple from the specimen as mentioned in the experiment section.

A representative microstructure obtained in this undercooling regime is shown in Fig. 3. The composition of the long needle-like structure is Pd_3Si and the matrix consists of Pd and Pd_5Si. The former is a dendritic crystallization while the latter is a eutectic solidification. The eutectic structure is not clearly shown in this micrograph. To illustrate it, a micrograph taken from the same undercooled specimen as in Fig. 3, but with larger magnification, is displayed in Fig. 4. The gray area at the upper right hand corner is a Pd_3Si dendrite. The matrix consists of Pd_5Si (background) and Pd (spheres). It is obvious from this micrograph that the matrix has a eutectic morphology. Returning to Fig. 3, since Pd_3Si appears as dendrites, they must have formed initially during solidification of molten $Pd_{80}Si_{20}$. Therefore, when reflecting on the temperature profile in Fig. 2, it is clear that the first crystallization peak refers to the dendritic growth while the second crystallization peak results from the eutectic solidification of the remaining liquid. It is interesting to note that at the boundaries of the Pd_3Si dendrite, there are Pd protrusions growing into the matrix (Please see Fig. 4 for details). It is therefore clear that the Pd_3Si are seeds for the crystallization of the eutectic structure Pd_5Si and Pd.

In the intermediate undercooling regime defined as $190\ K \leq \Delta T \leq 220\ K$, there are two crystallization peaks in a typical temperature profile. The thermal history of an undercooled specimen with the first peak occurring at $\Delta T = 210\ K$ is shown in Fig. 5. Their peak areas are about the same. After the appearance of the first crystallization peak, the second peak occurs randomly in the temperature range from the onset of the first peak to $\Delta T = 230\ K$. Again, mechanical test shows that the first peak corresponds

to partial crystallization of the original melt while the second peak refers to the crystallization of the remaining liquid.

The microstructures of an undercooled specimen solidified in this undercooling regime is shown in Fig. 6. Spherical morphologies, characteristics of nucleation and growth mode, are found all over the cross-section of the undercooled specimen. The large, somewhat darker round objects have a composition of Pd_3Si while those smaller, somewhat lighter in color, are Pd particles. The background has a composition of Pd_5Si. Compared with the microstructures in the least undercooling regime, there are three major differences and one similarity. The similarity is that Pd, Pd_3Si and Pd_5Si are again present. The three differences are discussed below.

Comparing the microstructures in Fig. 4 and 6, two obvious differences can be pinpointed immediately. First, in the least undercooling regime, Pd_3Si grows in dendritic form which is replaced by spherical morphology in the intermediate undercooling regime. Second, in the least undercooling regime the matrix is composed entirely of a eutectic structure of Pd and Pd_5Si while in the intermediate undercooling regime the matrix is mostly composed of large Pd precipitates embedded in Pd_5Si background and eutectic structure of Pd_5Si and Pd is scarcely found. The final difference is that Pd inclusions are found inside those spherical Pd_3Si of the intermediate undercooling regime as shown in Fig. 7 (this is the same undercooled specimen as shown in Fig. 6, but with larger magnification), but not a single inclusion can be identified in the Pd_3Si dendrites in the least undercooling regime.

There are three types of inclusions inside the spherical Pd_3Si. They are marked, respectively, by A, B and C as shown in Fig. 8. A and B are Pd_5Si and Pd inclusions, respectively. C has a more or less concentric structure with Pd enclosed inside a thin

layer of Pd_5Si. The origin of type A and C inclusions appears to be a result of coarsening. For instance, at D in Fig. 8, the Pd particle is in the process of being engulfed by Pd_3Si. However, it must be noted that the Pd and Pd_3Si are separated from each other by a thin layer of Pd_5Si. Another example is displayed at E in Fig. 8, which illustrates the engulfing of the Pd by Pd_3Si. It is noted that the Pd and Pd_3Si are separated from each other by a layer of Pd_5Si, which is more visible here than the one at D. This coarsening mechanism of course can be extended to explain the formation of A. However, an important consequence of this engulfing process is that the inclusion formed by this mechanism always contains Pd_5Si even if it is just a thin layer.

The engulfing process observed in the previous paragraph has been attributed to coarsening effect. To illustrate this point, a molten specimen was first undercooled to $\Delta T = 210$ K, the undercooling at which the undercooled specimen shown in Fig. 6 crystallized. Prolonged isothermal annealing was then applied to this molten specimen at $\Delta T = 210$ K until it crystallized. The microstructure of this undercooled specimen was shown in Fig. 9. It is obvious that connectedness has built up here while in Fig. 6, the islands are still quite independent of each other. The origin of the connectivity is due to coarsening [17].

The origin of the inclusion B shown in Fig. 8 will be clear after examining the microstructure in the largest undercooling regime discussed below.

In the largest undercooling regime, i.e. $\Delta T \geq 220$ K, there are either two overlapping peaks or very often just one crystallization peak. However, in both cases, the microstructures of the undercooled specimens are the same indicating that in the latter case, the two peaks are too close to each other to be resolved by the thermocouple. The microstructure of a typical undercooled specimen is shown in

Fig. 10. It displays a connected network. There are indeed two sub-networks in Fig. 10. The composition of the dark regions is Pd_5Si while that of the lighter areas is Pd_3Si. Those white spots are Pd particles. The final phases are therefore the same as those in the least and intermediate undercooling regimes. The characteristic wavelength of this connected structure is 0.8 μm. In general, the wavelength decreases with increasing undercooling. Compared with the characteristic size in Fig. 6, the characteristic wavelength in the largest undercooling is smaller by more than a factor of 30. In other words, there is a sudden refinement, by more than 30 times, in microstructure when crossing from the intermediate to the largest undercooling regime. The spread of the transition region is about 30 °C, which is quite narrow (please see the discussions section).

The white dots are Pd particles. They can be found either inside or on the surface of the Pd_3Si sub-network. For those Pd inclusions in the Pd_3Si sub-network, they are in direct contact with each other. No Pd_5Si layer is detected between them. Similarly, for those Pd attaching to outer surface of the Pd_3Si sub-network, there is no Pd_5Si layer found between the interface of Pd and Pd_3Si. In other words, it appears that these Pd particles and those B inclusions found in the intermediate undercooling regime may share a common origin.

In order to identify their origins, numerous Pd particles had been examined. In a few instances, a microstructure as shown in Fig. 11 is found. The white area in the micrograph is Pd, the dark region on the left is Pd_5Si and finally the gray area on the right is Pd_3Si. The point of interest in the micrograph is the diffused boundary between Pd and Pd_3Si. Since the color of the micrograph reflects qualitatively the local composition of the undercooled specimen, the micrograph in Fig. 11 indicates that

some Pd atoms are diffusing to the left to form the Pd precipitate, i.e. the Pd particle is formed by a diffusion process. A direct outcome is that the original composition of the Pd_3Si sub-network before solidification has a composition close to Pd_3Si, but slightly richer in Pd. Upon solidification, Pd precipitates out to allow for the solidification of the Pd_3Si sub-network.

Finally, according to Gibbs phase rule, the final crystalline undercooled specimen should contain only two phases. However, there are always three phases Pd, Pd_3Si and Pd_5Si present in all the as prepared undercooled specimen. It turns out that upon annealing of the undercooled specimens, Pd_5Si would decompose into Pd and Pd_3Si.

Discussions

In order to facilitate the discussions below, the phase diagram of Pd-Si [18] with the Pd rich portion is shown in Fig. 12.

For an undercooled specimen with the first crystallization peak falling in the least undercooling regime, its phases include crystalline Pd, Pd_3Si and Pd_5Si. The co-existence of crystalline Pd_3Si and an undercooled liquid below the solidus is not very surprising for the crystal structures of Pd_3Si [19] , Pd_5Si [19] and Pd are orthorhombic, monoclinic and face centered cubic, respectively. The very different crystal structure of Pd_3Si from the other two renders it an ineffective seed for the nucleation of crystalline Pd_5Si and Pd in the remaining undercooled liquid.

From the phase diagram in Fig. 12, it is not difficult to understand the dendritic precipitation in the least undercooling regime as shown in Fig. 3. As an undercooled molten $Pd_{80}Si_{20}$ is cooled below T_l but above the eutectic temperature T_e, the

equilibrium phase diagram informs us that upon crystallization, Pd_3Si precipitates out first. Meanwhile the composition of the remaining liquid becomes more and more Pd rich. When the temperature of the system is further cooled below T_e, as more Pd_3Si precipitates out, it is likely that the composition of the remaining undercooled liquid eventually enters the region of the phase diagram where the reaction is governed by the eutectic solidification of Pd and Pd_5Si to form the matrix.

When the onset of kinetic crystallization temperature T_k is below T_e but above 1023 K, the microstructures of an as obtained undercooled specimen are the same as those with T_k above T_e. It follows then that the transformation behavior discussed in the last paragraph also applies to the present case.

In the intermediate undercooling regime, the temperature profile displays two peaks. Mechanical test confirmed the existence of a solid-liquid mixture after the first crystallization peak, same as that in the least undercooling regime. Since the two peaks are of nearly equal magnitude, it is proposed here that the first peak corresponds to the crystallization of Pd_3Si (with Pd precipitation) and the second peak represents the crystallization of the Pd_5Si background with Pd precipitates (also with traces of eutectic structure of Pd and Pd_5Si), in line with the crystallization in the least undercooling regime.

Before analyzing the underlying transformations in the intermediate undercooling regime, it is necessary to trace the nature of the B-type inclusions inside the spherical Pd_3Si. Now the Pd precipitates inside the Pd_3Si sub-network in the largest undercooling regime and the B-type inclusions in the intermediate undercooling regime share one common property. In both cases, the Pd precipitates are in direct contact with Pd_3Si. There is no Pd_5Si between the two phases. Since the Pd particles in the

largest undercooling are formed by a diffusion process as shown in Fig. 11, it is proposed here that the B-type inclusions in the intermediate undercooling regime are also formed by a similar diffusion process. A direct consequence of this proposal is that before the formation of the spherical Pd_3Si in the intermediate undercooling regime, the original composition of the liquid in that region is close to Pd_3Si, but slightly rich in Pd. Upon solidification, as crystalline Pd_3Si forms, Pd precipitates out. This argument can also be used to explain the precipitation of Pd in the Pd_5Si matrix, i.e. the "remaining undercooled liquid" has a composition close to Pd_5Si, but richer in Pd. Crystallization requires the precipitation of Pd.

With this transformation mechanism in mind, the difference in the positions of the two crystallization peaks in the least and intermediate undercooling can be explained. In the former, after the appearance of the first peak, the second peak in most cases would not show up until $\Delta T \cong 230$ K. Besides, it is apparent that Pd_3Si acts as seed for the precipitation of Pd which finally leads to the crystallization of the whole specimen (Please see Fig. 4 for details). In the intermediate undercooling, after the first peak, the second peak appears randomly, rather independent of the degree of undercooling of the specimen. According to the proposed transformation mechanism, it is likely that during the first crystallization process, some of the Pd precipitates may find themselves attaching to the surface of the Pd_3Si. They are then seeds for the crystallization of the "remaining undercooled liquid". The appearance of Pd at the periphery of Pd_3Si is a random process, the second crystallization therefore must also appear randomly.

Comparing the Pd precipitates in the intermediate and largest undercooling regimes, there is one major difference. In the intermediate undercooling regime, plenty

Pd precipitates are found inside the Pd_5Si matrix. On the other hand, in the largest undercooling regime, the Pd precipitates are either found inside or attached themselves onto the surface of the Pd_3Si sub-network. No Pd precipitate has been found so far residing inside the Pd_5Si (Please see Fig. 10).

In the largest undercooling regime, in order to explain the absence of Pd precipitates in the Pd_5Si background, it is again necessary to reflect on the experimental findings in the least undercooling regime: The Pd_3Si is an effective seed for the "remaining undercooled liquid" for $\Delta T < 190$ K. The seeding mechanism is through the attachment of Pd onto the Pd_3Si surface (Again please see Fig. 4 for details). Now in the largest undercooling regime, the characteristic size of the network is very small. During crystallization of the Pd_3Si sub-network, Pd can be expelled, but still attached to the external surface of the Pd_3Si sub-network. Furthermore, it is assumed that the Pd_3Si sub-network crystallizes before that of Pd_5Si sub-network, in line with the crystallization behavior in the least and intermediate undercooling regimes. The "remaining undercooled liquid" (which has a composition close to Pd_5Si but richer in Pd) is now in contact with, in addition to Pd_3Si, also crystalline Pd. The latter can now act as seeds for the Pd inside the "remaining undercooled liquid". Now the wavelength of the network is only ~ 1 μm. All the Pd can then migrate from inside the still molten sub-network to the already crystallized Pd_3Si sub-network. Furthermore, it is apparent that a reduction of Pd content in the undercooled liquid promotes nucleation of the undercooled molten Pd_5Si. This explains the closeness of the two crystallization peaks in the temperature profile.

The morphology of an undercooled specimen crystallized in the highest undercooling regime exhibits a connected network which is a representative structure

of spinodal decomposition [20]. However, according to Ref. [17], connectedness is a necessary, but not sufficient condition for spinodal decomposition. Discrete particles, on annealing, can form a connected structure due to coarsening. Indeed, it was shown in the present studies that annealing can transform a microstructure clearly formed by nucleation and growth to a somewhat connected morphology although sharp corners have not been round off yet (Please see Fig. 6 and 9 for details). The critical test for spinodal decomposition lies in the building up or dying out of composition modulation. It was mentioned earlier in the introduction section that Chou and Turnbull [6] had used small angle x-ray scattering method to validate that the phase separation has occurred in amorphous Pd-Au-Si. Such a method, however, is useless in this work for the kinetics are too rapid and we cannot freeze the reaction momentarily to be studied by small angle x-ray scattering method. It appears that in order to understand the nature of the connected morphology in Fig. 10, we have to look for evidences elsewhere.

The undercooled specimens from both intermediate and largest undercooling regimes carry the same phases, namely Pd, Pd_3Si and Pd_5Si. We have determined experimentally that there is a sharp drop in the characteristic size of the microstructures at $\Delta T \sim 220$ K. The refinement in microstructures in a narrow temperature range cannot be explained in terms of the classical nucleation theory for the following reason: When an undercooled molten alloy had been purified thoroughly in advance, it can be undercooled to way below its T_l. Otherwise, undercoolability is always very limited. In the present studies, purified molten $Pd_{80}Si_{20}$ was cooled down slowly (8 K min^{-1}) and the maximum undercooling achieved was 300 K. Therefore, for those crystallizations with onset undercooling $\leq$ 300 K, they must be brought about

by heterogeneous impurities. Furthermore, the temperature profiles in Fig. 2 and 5 indicate that upon crystallization, the crystal growth velocity is still rapid enough to raise the overall temperature of the specimen to above the initial T_k. Then according to the classical nucleation theory, as a result of the increase in temperature of the undercooled molten specimen, the nucleation frequencies are reduced drastically due to its exponential dependence on temperature. Therefore, it is expected that the final microstructures of a purified undercooled specimens with $\Delta T < 300$ K is either a single crystal or a crystal with just a few grains. In other words, grain refinement is not anticipated in purified undercooled $Pd_{80}Si_{20}$ in accordance with the classical nucleation theory. The argument can be generalized to cases where intermediate metastable phases occur.

Grain refinement was first observed by Walker [21] in undercooled Ni. Later, it was extended to other systems as well [22, 23, 24]. Many proposals have been put forward, including re-melting [23] and dynamic nucleation [25], to explain this phenomenon. However, the most definitive experimental proof came only recently. Leung and Kui [26] demonstrated that grain refinement in Ni is brought about by dynamic nucleation. The characteristic features of grain refinement by dynamic nucleation in the sharp transition region are a gradual increase of grain size from a site where a void has just collapsed and the possible appearance of voids. Another possible mechanism leading to grain refinement is by re-melting of dendrites [27]. The characteristic features of this mechanism in the sharp transition region are composition inhomogeneity and fragments of dendrites broken up by re-melting. We have carried out detailed compositional and microstructural analysis in the transition region for the case of $Pd_{80}Si_{20}$. None of the characteristic features mentioned above is found.

Therefore, refinement in microstructures observed in undercooled $Pd_{80}Si_{20}$ must arise from a different source. In other words, the reactions leading to the microstructures in the intermediate and largest undercooling regimes are not the same even though the phases in the final products are the same. Now we have been able to rule out coarsening [17] as a possible mechanism for the connected structure. That leaves us only one choice: the connected network as shown in Fig. 10 is due to spinodal decomposition. In short, phase separation has been observed in undercooled $Pd_{80}Si_{20}$. The observed microstructures are also consistent with this conclusion. Nucleation and growth of the phase separation occurs in the intermediate undercooling regime while spinodal decomposition takes place in the largest undercooling regime.

One of the important questions left is whether the phase separation occurs in the undercooled liquid or in the solid state. If phase separation takes place in the solid state, both phase-separated phases (whether by nucleation and growth or spinodal decomposition) should have similar structures, e.g. same crystal structure [28]. Now the peaks in the temperature profile of continuous cooling experiment of molten $Pd_{80}Si_{20}$ are due to crystallizations. The as formed crystalline phases have very different crystal structures, i.e. they don't form the right couple for phase separation. Furthermore, no metastable intermediate solid state transformation has been recorded. Therefore, it can be concluded that the phase separation as observed in undercooled molten $Pd_{80}Si_{20}$ must have taken place in the undercooled homogeneous melt (The thermocouple was not sensitive enough to detect the heat evolved), subsequent crystallizations of the phase-separated undercooled melts lead to the two crystallization peaks. Since both of the crystallization peaks describe the transformations from melts to solids, they are of comparable magnitude after taking into account the relative

amount of each phase present in the undercooled specimen. Experimental data indicates that one of the phase-separated undercooled liquids has a composition close to Pd_3Si but slightly richer in Pd while the other one has a composition close to Pd_5Si but somewhat richer in Pd.

It should also be noted that the wavelength of the modulation in Fig. 10 is about 0.8 μm. It appears that this is far too long for solid state spinodal decomposition [29] where strain effect most likely cannot be ignored.

As mentioned earlier, there are two different kinds of transformations in phase separation which are nucleation and growth, and spinodal decomposition. The morphology in the intermediate undercooling regime is obviously due to nucleation and growth while the connected network in the largest undercooling regime is owing to spinodal decomposition. It would be interesting to see if the phase separation can be understood through the Pd-Si phase diagram. A hypothetical metastable miscibility gap is shown in Fig. 13. The values with composition $Pd_{80}Si_{20}$ are actual data. The actual data of other compositions will be published in another paper.

The microstructure structure of the matrix in Fig. 6 can now be explained in terms of the metastable miscibility gap as shown in Fig. 13. As a molten undercooled $Pd_{80}Si_{20}$ is undercooled into the miscibility gap where the transformation mechanism is governed by the nucleation and growth mode, the original homogeneous liquid is phase-separated into two undercooled liquids, say l_1 and l_2. It was found experimentally that l_2 solidifies into Pd_3Si and Pd. To understand the solidification behavior of l_1, the liquidus on the left hand side is extended into the metastable regime, which encloses l_1 or "the remaining undercooled liquid". Upon solidification, according to the phase diagram, precipitation of Pd should take place first. The precipitation

reaction in this case proceeds with a planar interface in contrast to dendritic growth of the Pd_3Si precipitates in the least undercooling regime. Meanwhile the composition of the remaining liquid would be pushed to the eutectic composition (of Pd and Pd_5Si). Consequently, eutectic structure of Pd and Pd_5Si is also observed.

It is interesting to reflect on the glass forming ability of Pd-Si in the light of the liquid state phase separation. Earlier, when formulating the glass forming ability of an alloy glass, liquid state phase separation is not anticipated. However, composition analysis in this work reveals that the compositions of the spinodal liquids are different from that of the original homogeneous liquid, $Pd_{80}Si_{20}$. Even worse, according to the metastable miscibility gap in Fig. 13, with decreasing temperature, the composition of one of the spinodal liquids would move closer and closer to Pd_3Si which is a stoichiometric compound with high melting temperature. Consequently, the reduced undercooling defined as $(T_l - T)/T_l$ is much higher for the newly formed spinodal liquid. This of course implies that the glass forming ability of the system is much reduced [2].

We thank Research Grants Council of Hong Kong for financial support.

References

1. M.H. Cohen and D. Turnbull, Nature 189, 131 (1961).
2. M. Marcus and D. Turnbull, Mat. Sci. and Eng. 23, 211 (1976).
3. D. Turnbull, Contemporary Physics 10, 473 (1969).
4. D. Turnbull, The 1980 Campbell Memorial Lecture, The American Society for Metals, Metallurgical Transactions A, 12A, 695 (1981).
5. H.S. Chen and D. Turnbull, Acta Metall. 17, 1021 (1969).
6. C.-P. Chou and D. Turnbull, J. Non-Cryst. Sol. 17, 169 (1975).
7. H.S. Chen, Mater. Sci. Engng. 23, 151 (1976).
8. L.E. Tanner and R. Ray, Scr. Metall. 14, 657 (1980).
9. M.C. Lee and W.L. Johnson, Appl. Phys. Lett. 41, 1054 (1982).
10. D. Deng and A.S. Argon, Acta Metall. 34, 2011 (1986).
11. R. Gerling, F.P. Schimansky, and R. Wagner, Nuclear Sci. Engng. 110, 374 (1992).
12. M.J. Regan and A. Bienenstock, Phys. Rev. B 51, 12170 (1995).
13. M.B. Fernandez van Raap, F.H. Sanchez, and Y.D. Zhang, J. Mater. Res. 10, 1917 (1995).
14. H.W. Kui, A.L. Greer, and D. Turnbull, Appl. Phy. Lett. 45, 615 (1984).
15. C.F. Lau and H.W. Kui, J. Appl. Phys. 67, 3181 (1990).
16. C.F. Lau and H.W. Kui, J. Appl. Phys. 73, 2599 (1993).
17. T.P. Seward, D.R. Uhlmann, and D. Turnbull, J. Am. Ceram. Soc. 51, 634 (1968).
18. *Binary Alloy Phase Diagrams*, edited by B.T. Massalski (American Society for Metals, Metals Park, OH, 1993).
19. J. Wysocki and P. Duwez, Metall. Trans. A 12, 1455 (1981).

20. J.W. Cahn, J. Chem. Phys. 42, 93 (1965).

21. J.L. Walker, *Principles of Solidification*, edited by B. Chalmers (Wiley, New York, 1964), p.112.

22. T.Z. Kattamis and M.C. Flemings, Trans. AIME 236, 1523 (1966).

23. G. Devaud and D. Turnbull, Acta Metall. 35, 765 (1987).

24. C.F. Lau and H.W. Kui, Acta Metall. Mater. 39, 323 (1991).

25. G. Horvay, International Journal of Heat and Mass Transfer 8, 195 (1965).

26. K.K. Leung, C.P. Chiu, and H.W. Kui, Scr. Metall. Mater. 32, 1559 (1995).

27. J.Z. Xiao, K.K. Leung, and H.W. Kui, Appl. Phys. Lett. 67, 3111 (1995).

28. J.W. Cahn, Trans. Met. Soc. AIME 242, 166 (1968).

29. J.E. Hilliard, *Phase Transformations*, American Society for Metals, Metals Park, Ohio, 1970, p.497.

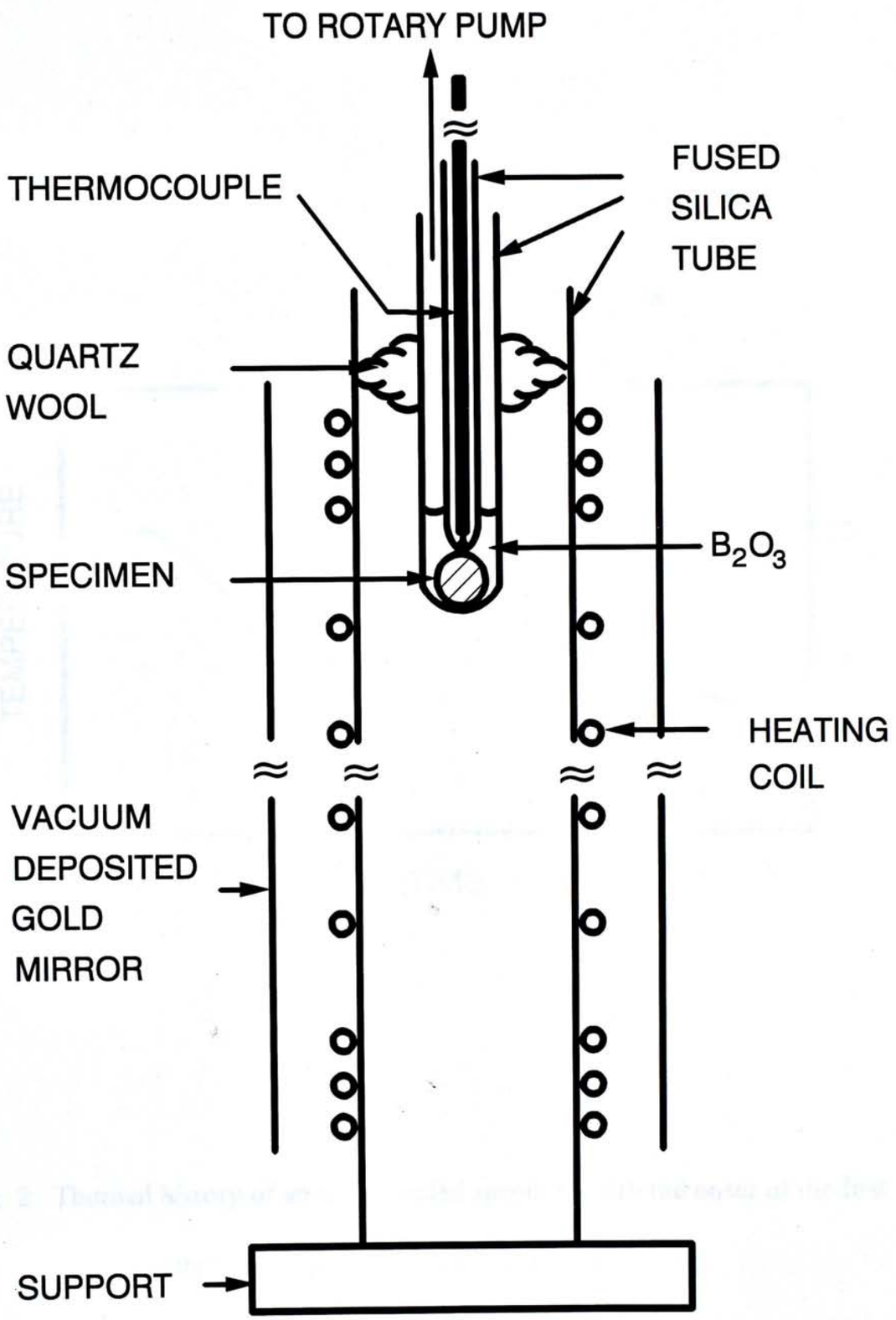

Fig. 1 Schematic diagram of the undercooling experiment.

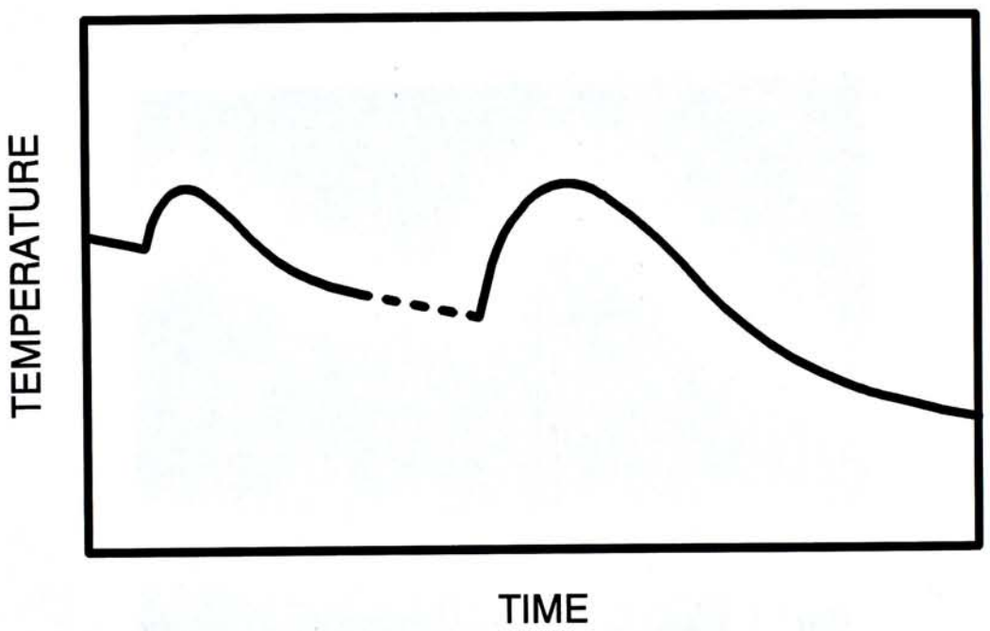

Fig. 2 Thermal history of an undercooled specimen with the onset of the first crystallization peak occurring in $0 \leq \Delta T \leq 190$ K.

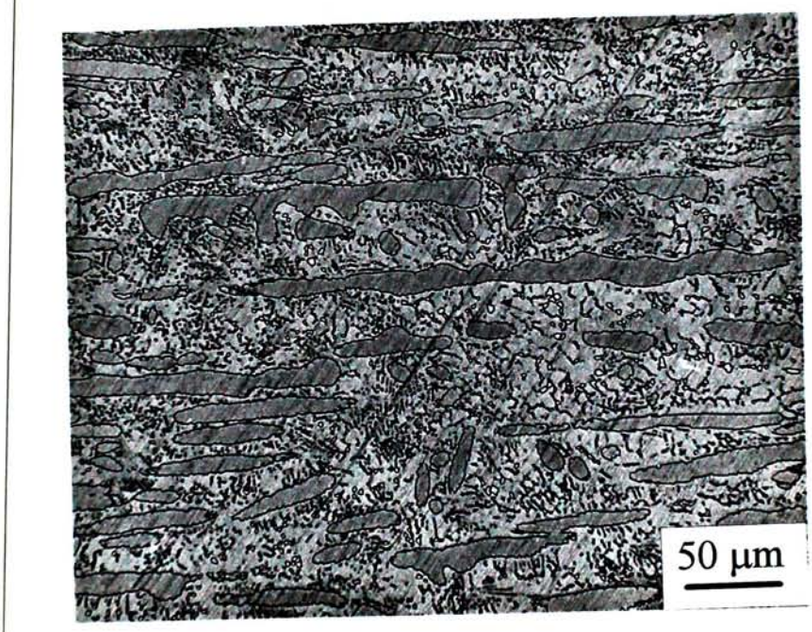

Fig. 3 Micorstructure of an undercooled specimen that crystallized inside $0 \leq \Delta T \leq$ 190 K. It displays the dendritic precipitation of Pd_3Si (the long needles). The matrix consists of Pd_5Si, and eutectic structure of Pd_5Si and Pd.

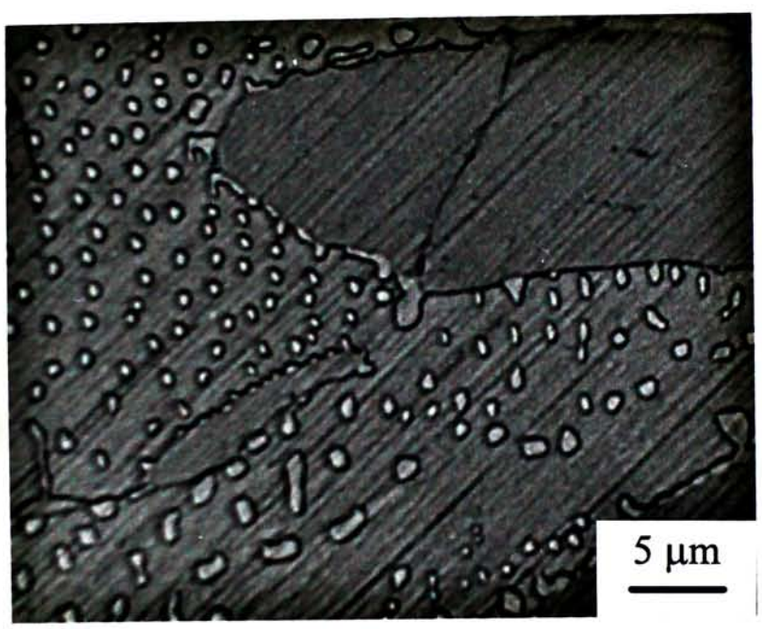

Fig. 4 Enlarged micrograph of the same undercooled specimen as shown in Fig. 3. It illustrates the eutectic structure of Pd (dots) and Pd_5Si. Note the Pd_3Si dendrite at the upper right hand corner is surrounded by Pd at its boundary.

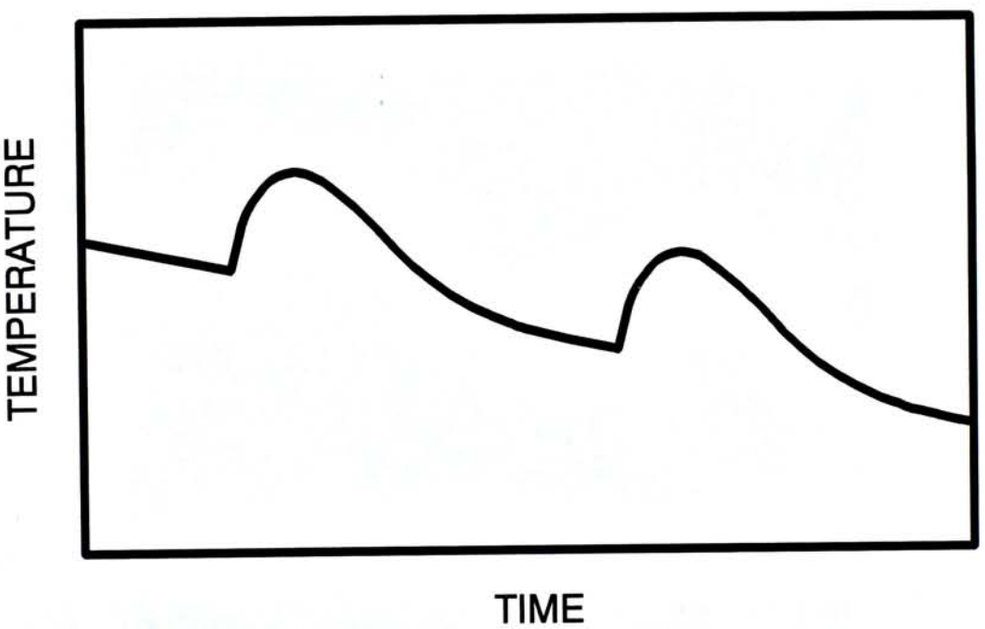

Fig. 5 Thermal history of an undercooled specimen with $\Delta T = 210$ K. It shows two crystallization peaks.

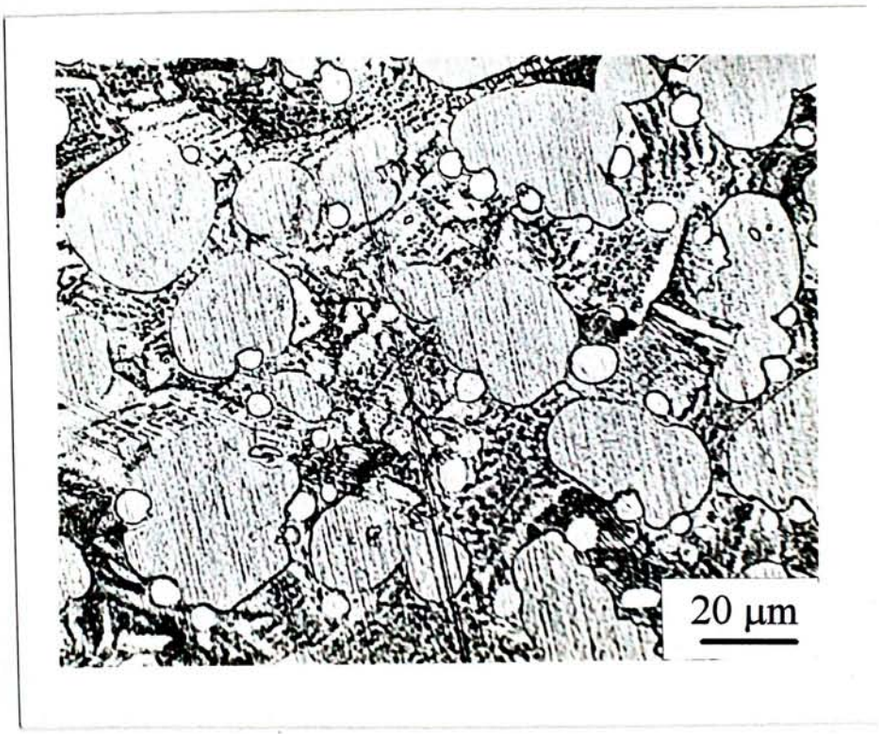

Fig. 6 Microstructure of an undercooled specimen with $\Delta T = 210$ K. The morphology obviously originates from nucleation and growth.

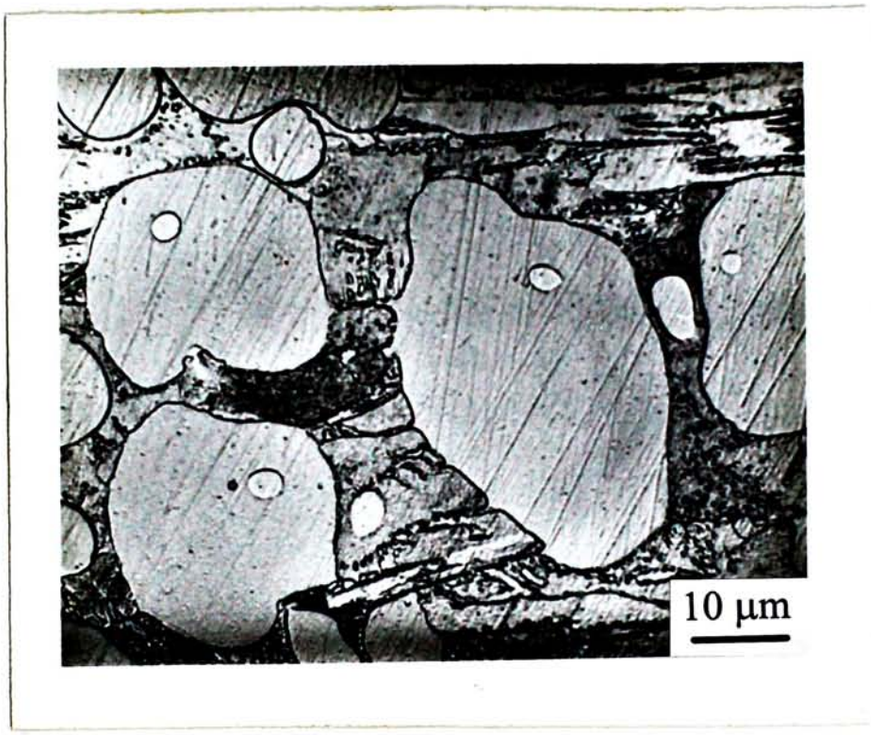

Fig. 7 An enlarged micrograph of the undercooled specimen shown in Fig. 6 showing the Pd precipitates inside the Pd_3Si.

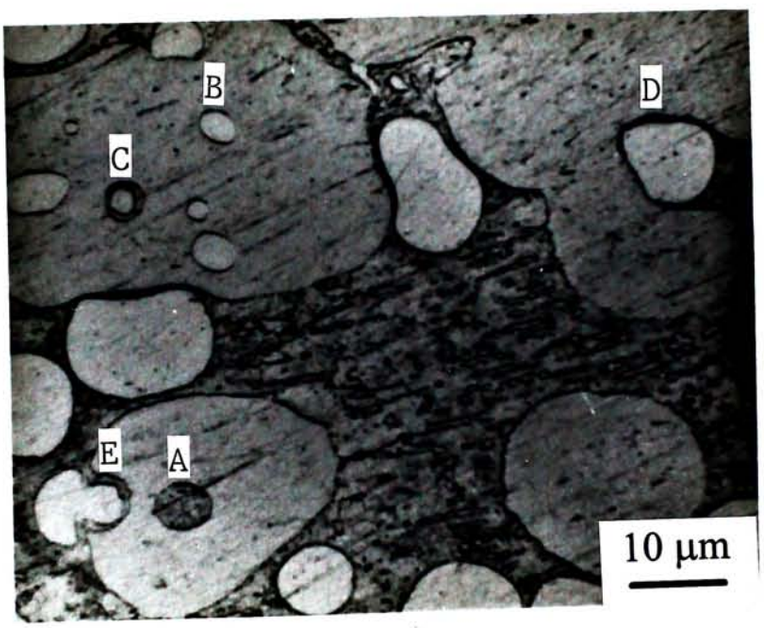

Fig. 8 The different types of inclusions inside the Pd_3Si.

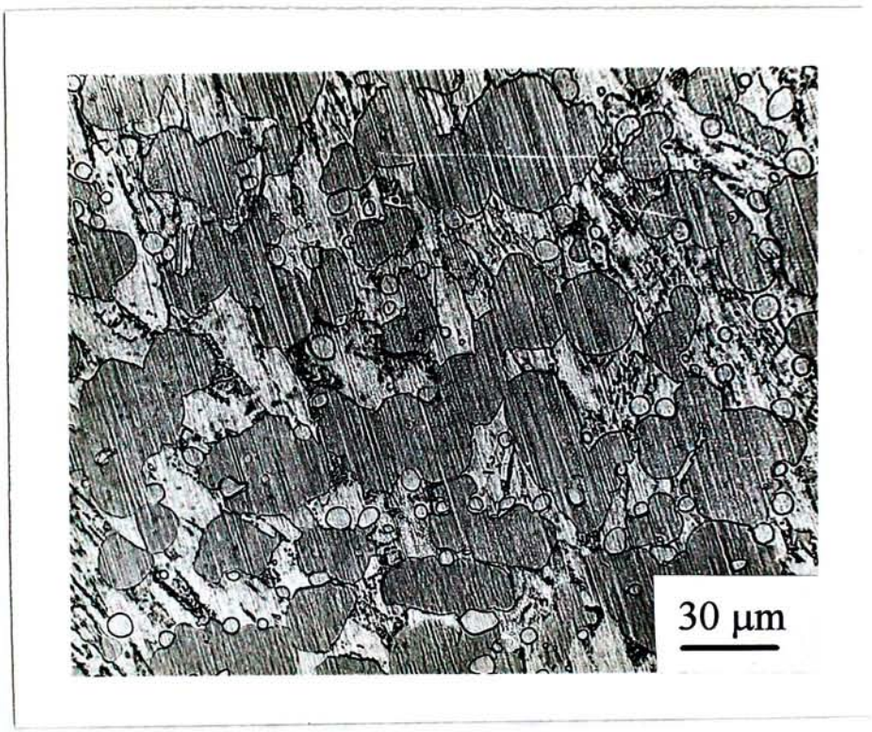

Fig. 9 Microstructure of an undercooled specimen that had been annealed in the liquid state at $\Delta T = 210$ K for a prolonged period before crystallized. It depicted a connected structure originates from coarsening.

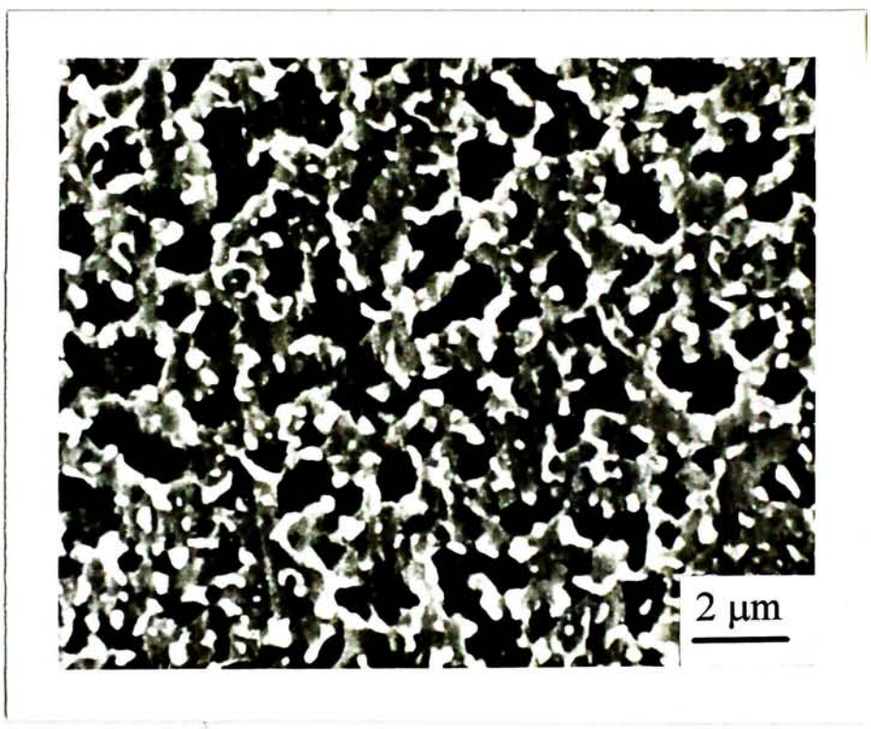

Fig. 10 Typical microstructure of an undercooled specimen that crystallized with $\Delta T \geq 220$ K. A connected network made of two sub-networks is found.

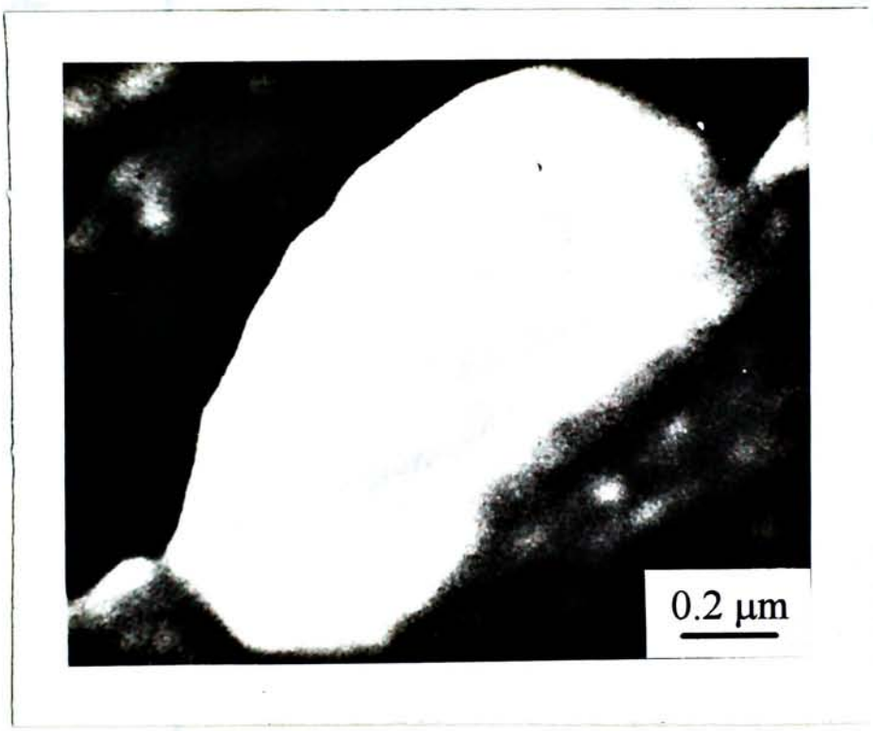

Fig. 11 Micrograph showing the formation of Pd precipitation in the largest undercooling regime. Since the degree of darkness represents qualitatively the local composition, it is clear that the Pd precipitate is formed by a diffusion process.

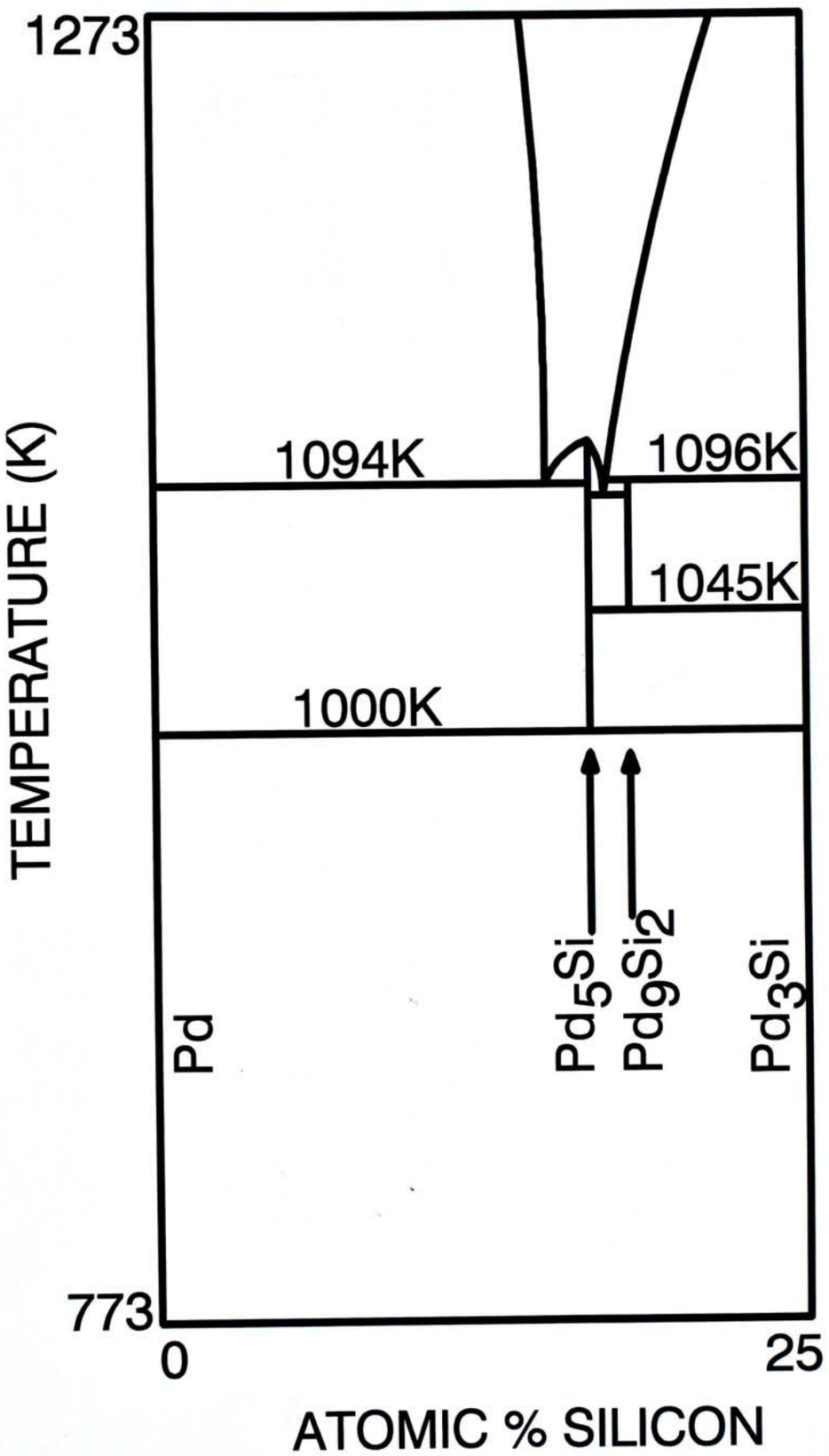

Fig. 12 Pd-Si phase diagram showing the Pd rich portion.

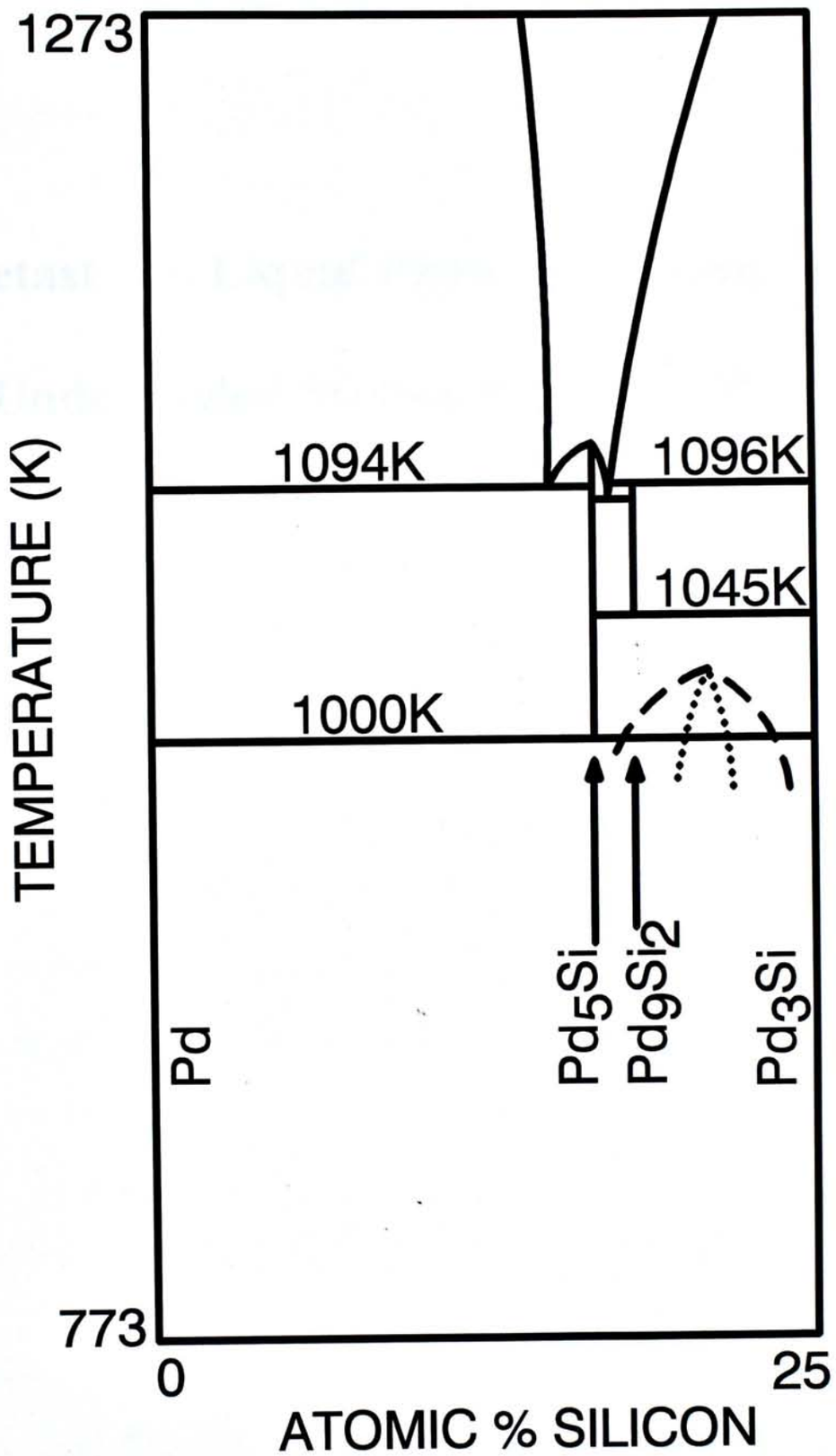

Fig. 13 Portion of the Pd-Si phase diagram including a hypothetical metastable liquid miscibility gap which is the origin of the phase separation reaction.

Chapter Three

Metastable Liquid Phase Separation in Undercooled Molten $Pd_{40.5}Ni_{40.5}P_{19}$

(submitted to J. Mater. Res.)

Metastable liquid phase separation in undercooled molten $Pd_{40.5}Ni_{40.5}P_{19}$

C.W. Yuen, K.L. Lee and H.W. Kui

Department of Physics, The Chinese University of Hong Kong

Shatin, N.T., Hong Kong

Abstract

It was demonstrated that molten $Pd_{40.5}Ni_{40.5}P_{19}$ undergoes liquid state phase separation in the undercooling regime $\Delta T = T_l - T$ where T_l is the liquidus of $Pd_{40.5}Ni_{40.5}P_{19}$ and T is the kinetic crystallization temperature. Liquid state phase separation by nucleation and growth takes place for $\Delta T \leq 60$ K while that by spinodal decomposition occurs for $\Delta T \geq 100$ K. For $60 \leq \Delta T \leq 100$ K, microstructure indicates that it is the no-theory regime. Finally, during liquid state spinodal decomposition, a system consisting of two liquid network appears initially, which is replaced subsequently by a system of three liquid networks before crystallization.

Recently, Lee and Kui [1] demonstrated that molten $Pd_{80}Si_{20}$ undergoes metastable liquid state phase separation (MLPS) in the undercooling regime defined as $\Delta T = T_l - T$ where T_l is the liquidus of $Pd_{80}Si_{20}$ and T is the kinetic crystallization temperature. There are two mechanisms for MLPS which are metastable liquid state phase separation by nucleation and growth (MLNG), and by spinodal decomposition (MLSD). Physically, MLPS is possible in undercooled molten $Pd_{80}Si_{20}$ for two reasons. First, it is a eutectic alloy and there is apparent partial miscibility in the liquid state deep in the undercooling regime. Second, it can be undercooled to a temperature regime where the partial miscibility is revealed.

Chen [2], through thermal analysis by a differential scanning calorimeter (DSC), found that glassy $Pd_{40.5}Ni_{40.5}P_{19}$ specimens undergo partial phase separation as they are heated up from below the glass transition temperature T_g to just slightly above T_g. Further heating would lead to crystallization. Since the phase separation is far from completion, it is difficult to draw meaningful conclusions. In this study, MLPS was investigated by reversing the process: Molten specimen, after purification, was undercooled to way below its liquidus to allow the phase-separation reaction to take place. Recently, Chen [3] had predicted the occurrence of two intermediate spinodal networks before the appearance of the final three spinodal networks for a ternary spinodal system. The ternary alloy $Pd_{40.5}Ni_{40.5}P_{19}$, due to its high resistance to crystallization [4], is an ideal system in confirming the prediction. In this paper, we report the MLPS in undercooled molten $Pd_{40.5}Ni_{40.5}P_{19}$.

$Pd_{40.5}Ni_{40.5}P_{19}$ specimens were prepared by first melting Ni_2P powder (99.9% pure) in a clean fused silica tube under a vacuum of ~ 10^{-3} Torr. The resulting ingots were then put into another clean fused silica tube together with weighed Pd and Ni granules.

Alloying was brought about by rf induction heating under Ar atmosphere. The undercooling of molten $Pd_{40.5}Ni_{40.5}P_{20}$ was achieved by fluxing the molten specimen in molten anhydrous B_2O_3 at an elevated temperature [4].

The crystallization experiments were carried out in a Transtemp furnace which is mainly composed of a heating coil surrounded by a Au plated fused silica tube. Since the Au coating is very thin, solidification process can be observed directly. The heating/cooling rates of the Transtemp furnace is controlled by a personal computer.

In the experiment, $Pd_{40.5}Ni_{40.5}P_{19}$ ingots and anhydrous boron oxide were put in a clean fused silica tube of outer diameter 11 mm. Then the inside of the fused silica tube was evacuated by a mechanical pump to ~ 10^{-3} Torr. Next the specimen and the boron oxide, both residing at the bottom of the fused silica tube, were heated up to ~ 1273 K by a torch. The high temperature heat treatment was maintained for ~ 4 hr to facilitate the removal of heterogeneous impurities from the molten specimen. The temperature of the molten specimen was read by a thermocouple, which was sheathed by another clean fused silica tube of outer diameter 4 mm, immersing inside the molten specimen. The thermocouple which was used to record crystallization was connected to a X-T plotter. The experimental details can be found in Ref [4].

After the heat treatment, the whole system was transferred to the Transtemp furnace which was preset at 1173 K, well above the T_l of $Pd_{40.5}Ni_{40.5}P_{19}$ (=935 K). We waited for about 20 min. to ensure thermodynamic equilibrium before starting a cooling cycle at a rate of 8 K/min. The thermal history including crystallization was recorded by the thermocouple described above.

For $\Delta T \leq 60$ K, upon solidification the thermocouple recorded two overlapping peaks. The whole crystallization period lasted about 40 s. The crystallizing molten

specimen as viewed through the Transtemp furnace remained shiny after the first peak, but turned blurred after passing through the second peak. In order to confirm the physical state of the specimen after the first crystallization peak, in a separate run, a clean fused silica rod was used to stir the specimen during the entire crystallization process. We found that at the end of the first crystallization peak, stirring was still possible indicating that the specimen was partly molten. However, the specimen was quite viscous. In fact, during stirring, small pieces of solids could be brought out onto the surface of the specimen confirming that the specimen was a mixture of liquid and small crystalline precipitates. On the other hand, after passing through the second peak, the specimen became a solid for the fused silica tube could no longer penetrate it. The microstructure of a typical undercooled specimen obtained in this undercooling regime is shown in Fig. 1. It depicts two dendritic systems. The large, bone-like dendrite has a composition of $Pd_{30}Ni_{45}P_{25}$ by EDX analysis. In the following discussions, they are denoted by α. The composition of the smaller dendrites (those with broken branches) is $Pd_{40}Ni_{60}$ and they are denoted by β. Basically, these two dendritic systems are independent of each other for their orientations have no correlation. It is noted that most of the β dendrites are located between the larger α dendrites. Furthermore, there are many β dendrites attaching to the tips of the side branches of a α dendrite. It can therefore be concluded that the α dendrite is a seed for the β dendrite.

The environments of the α and β dendrites are very different. The α dendrites are surrounded by a ternary eutectic, for example, the region indicated by a white arrow lying right next to the α dendrite as shown in Fig. 2. The ternary eutectic consists of $Pd_{30}Ni_{45}P_{25}$ or α (dark lines), $Pd_{40}Ni_{60}$ or β (white lines) and $Pd_{70}Ni_8P_{22}$ or γ (background black

patches). These phases are similar to that found in undercooled $Pd_{40}Ni_{40}P_{20}$ as reported in Ref [5].

The β dendrites are surrounded by a binary eutectic which in turn is surrounded by a thin layer at its outer boundary. A typical example, which is indicated by a white arrow, is shown in Fig. 2. The binary eutectic consists of $Pd_{70}Ni_8P_{22}$ or γ (dark patches) and $Pd_{40}Ni_{60}$ or β (white lines). The third phase at the rim as shown in Fig. 2 is α.

Now we have two independent dendritic systems which are surrounded by different eutectics and there are two overlapping crystallization peaks. The solidification mechanism and microstructures can only be explained as follows: In this undercooling regime, the original homogeneous undercooled liquid has phase-separated into two undercooled liquids, denoted by l_1 and l_2, respectively. Upon crystallization, α dendrites grow, say, in l_1 first. They trigger the crystallization of β dendrites as soon as the tip of the growing α dendrites touch a neighboring l_2 liquid droplet. The heat released from α and β gives rise to the first crystallization peak. The remaining part of the specimen at this moment is still molten. This explains why after the first crystallization peaks, the specimen still has a shiny surface and we could stir it with a fused silica rod. However, the α and β dendrites can act as seeds for the remaining liquids resulting in the ternary eutectics and the binary eutectics (with the third phase at the boundary), respectively which exhibit themselves in the second crystallization peak in the thermogram. The details will be discussed in another paper.

In Fig. 1, the size of the dendrite is very large, esp. the α dendrites. In addition, there is no spatial alternation of the α and the β dendrites, i.e. no network morphology. It can therefore be concluded that the MLPS as observed above must have taken place by nucleation and growth, i.e. MLNG. The MLNG also implies that there is no complete

miscibility in the metastable liquid. If the free energy curve of the undercooled liquid vs composition is a smooth curve, such as that of the free energy curve of the liquid phase in monotectic system, microstructures that are characteristic of spinodal decomposition should be revealed in the somewhat deeper undercooling regime. In the following, such microstructures are shown and discussed.

For $60 \leq \Delta T \leq 100$ K, the microstructure of a typical undercooled specimen consists of two networks of different compositions and tiny islands. The micrograph of a typical island together with its neighboring networks is shown in Fig. 3. Except near the boundary, the composition of the island is $Pd_{30}Ni_{45}P_{25}$ or α. A concentration gradient is found at the boundary between the island and its neighboring networks, which is qualitatively reflected by the degree of darkness at that region as shown in the micrograph. The dimension of the α islands is substantially larger than its neighboring network which are almost of uniform size ruling out the possibility that α-island formation is due to coarsening. It is apparent that the α islands are dendritic in nature, same as those of the α dendrite in the undercooling regime with $\Delta T \leq 60$ K. It is noted that the coexistence of tiny nuclei and spinodal networks, and the concentration gradient at the interface of the nuclei and their neighboring networks are the characteristic features in the diffuse transition regime from nucleation and growth to spinodal decomposition [6, 7, 8, 9].

For $100 \leq \Delta T \leq 160$ K, the characteristic microstructure is a purely random connected network. The microstructure of an undercooled specimen that crystallized at $\Delta T = 100$ K is displayed in Fig. 4. It depicts two networks intermixing with each other. The characteristic wavelength is ~ 0.5 μm. The compositions of the two networks are $Pd_{37}Ni_{42}P_{21}$ (grayish white) and $Pd_{47}Ni_{38}P_{15}$ (black), respectively and they are different from those observed in the undercooling regime, $\Delta T \leq 60$ K.

An undercooled specimen that was prepared by continuous cooling with $\Delta T = 150$ K is shown in Fig. 5. Three networks are identified and the overall dimension of the system is substantially reduced when comparing with that in Fig. 4. The compositions of the three networks are β, γ and $Pd_{35}Ni_{40}P_{25}$ (denoted by α'), respectively. In the least undercooling regime, $\Delta T \leq 60$ K, the stable crystalline phases are α, β and γ, respectively. α and α' deviate only slightly from each other. Compared with the undercooled specimen in Fig. 4, the undercooled specimen shown in Fig. 5 had undergone a longer period of annealing in the metastable liquid state. It is apparent that with sufficient annealing time, the two networks shown in Fig. 4 would decompose into three networks as predicted by Chen [3] for a ternary system. In other words, the composition/phases observed in Fig. 4 are the intermediate states. The detailed decomposition behavior will be discussed in another paper.

Based on the morphologies observed for undercooled specimens with $\Delta T \geq 60$ K, it is concluded that metastable liquid state spinodal decomposition MLSD also takes place in undercooled molten $Pd_{40.5}Ni_{40.5}P_{19}$.

We thank Research Grants Council of Hong Kong for financial support.

References

1. K.L. Lee and H.W. Kui, to be published.
2. H.S. Chen, Mater. Sci. Eng. 23, 151 (1976).
3. L.Q. Chen, Acta Metall. et Mater. 42, 3503 (1994).
4. H.W. Kui, A.L. Greer and D. Turnbull, Applied Physics Letters 45, 615 (1984).
5. P.E. Donovan, P.V. Evans, and A.L. Greer, J. Mater. Sci. Lett. 5, 951 (1986).
6. J.S. Langer, Physica 73, 61 (1974).
7. K. Binder, Phys. Rev. A 29, 341 (1984).
8. H. Tanaka, Phys. Rev. Lett. 65, 3136 (1990)
9. J. Jayalakshim, B. Khalil, and D. Beysens, Phys. Rev. Lett. 69, 3088 (1992).

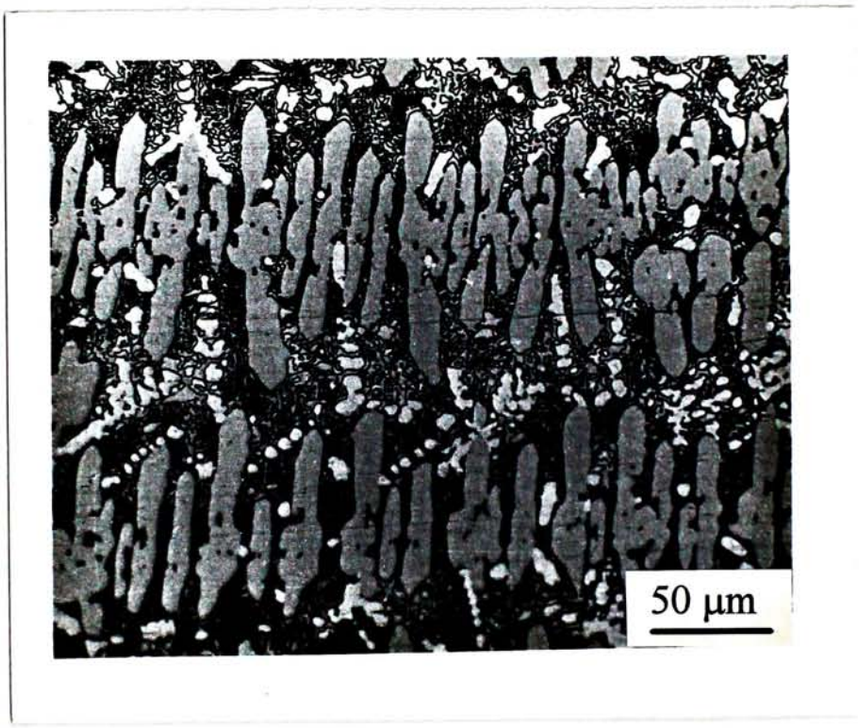

Fig. 1 Cross-section of a typical undercooled specimen in the undercooling regime with $\Delta T \leq 60$ K showing two different dendritic systems.

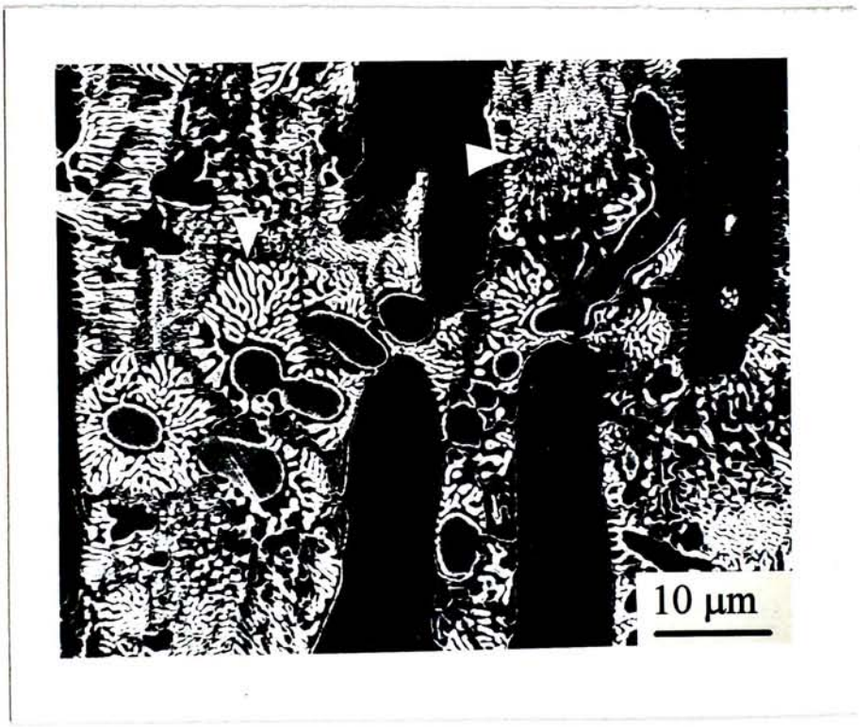

Fig. 2 SEM micrograph depicting that the α dendrite is surrounded by a ternary eutectic while the β dendrite is surrounded by a binary eutectic with a third phase at the rim.

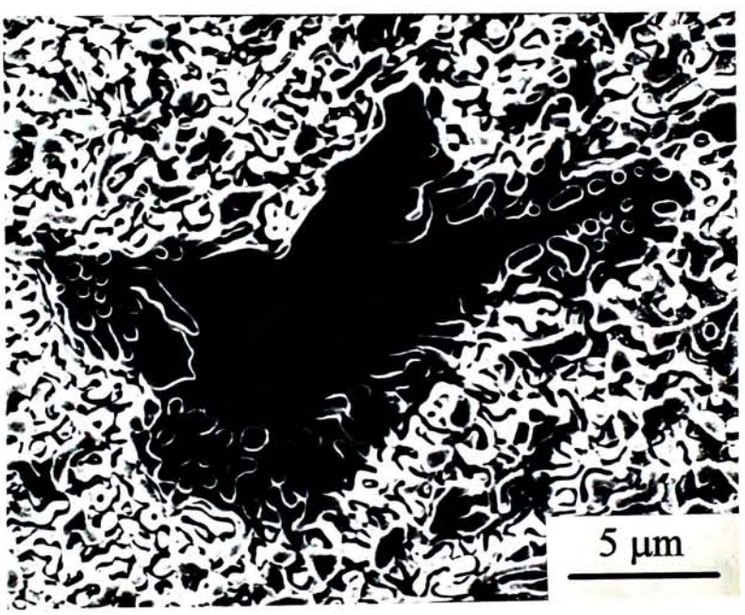

Fig. 3 A tiny nucleus immersed in connected networks in the diffuse transition region.

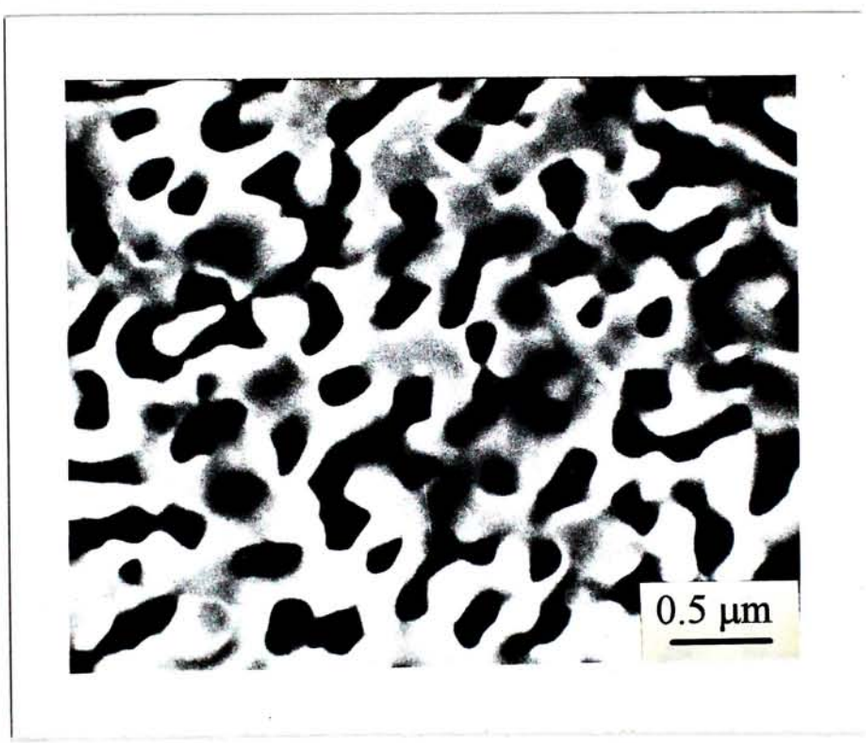

Fig. 4 Cross-section of an undercooled specimen with $\Delta T = 100$ K displaying the two networks intermixing with each other.

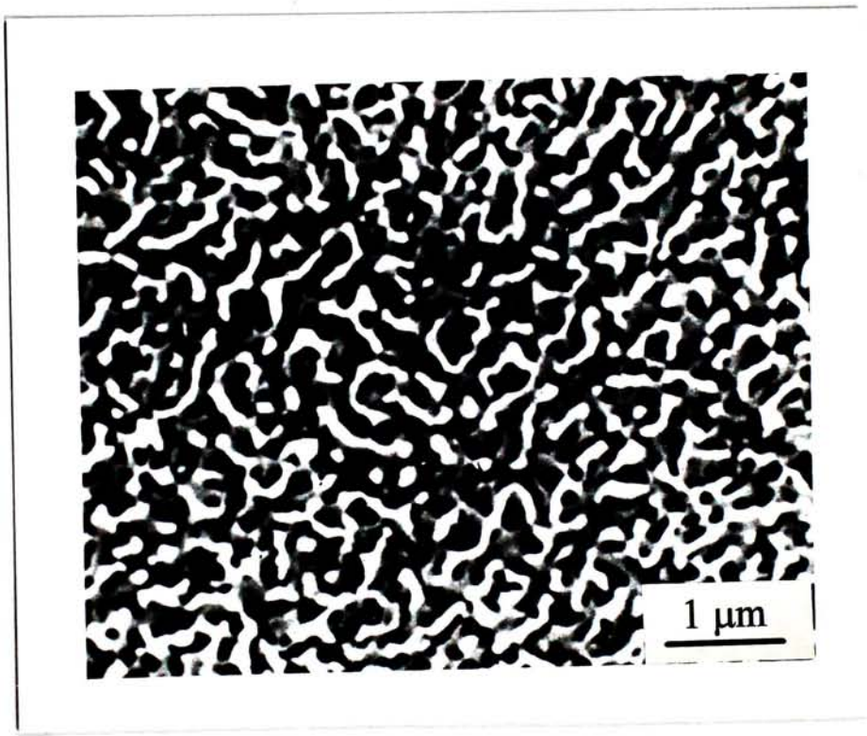

Fig. 5 An undercooled specimen with $\Delta T = 150$ K showing three connected networks. The microstructures are much finer.

Chapter Four

Crystallization of Spinodal Decomposed Melts of $Pd_{80}Si_{20}$

Introduction

Recently, it was demonstrated that when molten $Pd_{80}Si_{20}$ alloy [1] and $Pd_{40.5}Ni_{40.5}P_{19}$ [2] alloy are undercooled to way below their liquidus T_l, liquid phase separation occurs both by nucleation and growth and spinodal decomposition.

Liquid phase separation is expected to occur in these alloys for they are eutectic systems, that is, the enthalpies of mixing are positive. At high temperatures, the negative entropic contribution to the free energy of mixing forces complete mixing of the constituent atoms in the melt. However, when the temperature is low enough, the positive enthalpy of mixing dominates, resulting in the clustering of the same species of the constituent atoms in the highly undercooled liquid state. Even so, phase separation still cannot have enough time to proceed if the melt is quenched too rapidly to the glass state. Therefore, phase separation can occur at low enough temperatures only when the kinetic condition is favourable, for example, when the quenching rate is slow.

In the undercooling experiments of $Pd_{80}Si_{20}$ alloy [1] and $Pd_{40.5}Ni_{40.5}P_{19}$ alloy [2], we employed the glass fluxing technique [3] to purify the melt so as to achieve high undercoolings with a slow cooling rate (8 K/min) to bring about the occurrence of the liquid phase separation. For $Pd_{80}Si_{20}$, we found that when a homogeneous melt is undercooled by ΔT where $190\ K < \Delta T < 220\ K$, it would phase separate into two liquid phases by nucleation and growth, giving rise to spherical morphologies on solidification. At higher undercoolings where $\Delta T > 220\ K$, the homogeneous melt would phase separate into two interconnected liquid phases by spinodal

decomposition. As a result, a metastable liquid miscibility gap was proposed, which is plotted on the Pd-Si phase diagram as shown in Fig. 13 in chapter two.

The metastable spinodal liquid structure is a novel structure in metallic system. It is interesting to study the crystallization behavior of this phase separated liquid. In this chapter, the crystallization of $Pd_{80}Si_{20}$ spinodal liquids was studied.

Experimental

The experimental procedure is basically the same as described in chapter two. Only a brief description is given here. Elemental Pd and Si ingots, weighed in right proportion, were put into a clean fused silica tube and alloying was brought about by radio frequency (rf) induction heating. In the experiment, the $Pd_{80}Si_{20}$ ingot as prepared and anhydrous B_2O_3 (fluxing agent) were inserted into a clean fused silica tube. The tube was maintained at a vaccum of ~10^{-3} Torr by a mechanical pump and the whole system was heated at a temperature of ~1400 K by a torch for about 4 h to purify the molten specimen. Then it was transferred into a furnace pre-set at 1273 K, well above the liquidus of $Pd_{80}Si_{20}$. The temperature of the specimen was detected by a thermocouple which was sheathed by another small fused silica tube and inserted into the specimen. After the establishment of thermal equilibrium between the molten specimen and the furnace, the furnace was allowed to cool down at a rate of 10 K/min until the molten specimen crystallized. Then the specimen was taken out from the furnace and cooled to room temperature. The specimen was cut, polished and etched

in an etchant of $HCl:HNO_3:H_2O$ = 5:1:3. The microstructure of the specimen was examined by optical and electron microscopy.

Results

According to our previous result [1], the critical temperature of the spinodal region of $Pd_{80}Si_{20}$ is 993K, or ΔT = 220K. In order to study the crystallization of the spinodal decomposed melt, a series of undercooled specimens were prepared with the onset of kinetic crystallization temperature T_k lower than 993 K, that is, $\Delta T > 220$ K. The largest undercooling achieved (before the crystallization) was 300 K. The recalescence peaks in the temperature profiles of the specimens due to the latent heat released on crystallization are either a single peak or occasionally two overlapping peaks. No heat released due to the liquid spinodal decomposition is detected in the temperature profiles. The duration of the crystallization process is about 1 s or less. Under optical microscope (x 1000), the surfaces of the as formed specimens display an isotropic fine structure of two interconnected phases. After cutting, polishing and etching, the cross-sections of these specimens show a microstructure composed of coarse grains with a fine network structure overlapping on them. In a few specimens, the coarse grains form a radial dendritic pattern. Details of these microstructures are described as follows.

The cross-section of a typical specimen crystallized at ΔT = 280 K exhibits a characteristic isotropic spinodal structure, as shown in Fig. 1. By EDX analysis, the connected network is found to be Pd_3Si and the background is Pd_5Si. The white dots

scattering on the network are pure Pd. The dimensions of the network is about 1 μm. This structure of Pd_3Si network covers most of the cross-sectional area of the specimen. The orientation of the branches of the network is basically isotropic, but a bit alignment of the branches is occasionally observed in a few locations of the cross-section. The white Pd spots distribute inside or at the edge of the Pd_3Si network, but not inside Pd_5Si. The Pd_5Si background is made up of much larger grains which can be recognized under low magnification, as shown in Fig. 2, in which the large Pd_5Si grains superpose with the fine structure of Pd_3Si network. The sizes of the grains range roughly from 0.1 mm to 1mm. The shapes and the boundaries of the grains are quite irregular.

Fig. 3 is the magnified picture of Fig. 2 showing the grain boundary. The darker and the lighter portions correspond to two different grains of Pd_5Si. The structure of the network of Pd_3Si appears to be independent of the grain boundary of Pd_5Si. The network of Pd_3Si is not broken or distorted by the grain boundary of Pd_5Si. Indeed, it crosses the boundary freely. Therefore, it is obvious that the Pd_3Si network crystallizes before the solidification of Pd_5Si. This is in accordance with our previous observation in the temperature regime above the spinodal region that the crystallization of Pd_3Si always precedes that of Pd_5Si [1].

In two particular specimens that crystallized at $\Delta T = 260K$ and $\Delta T = 270K$, the cross-sections display a radial dendritic structure of Pd_5Si grains as shown in Fig. 4. Under high magnification, the structure of the Pd_3Si network is basically the same as that in Fig. 1, but somewhat aligns radially (discussed in the next paragraph). Since

there is a radial symmetry for both phases Pd_5Si and Pd_3Si, the center of the radial structure in Fig. 4 is therefore the origin of solidification for both phases. On the other hand, the Pd_3Si network can also cross the grain boundaries of the Pd_5Si dendrites freely as in Fig. 3. Hence, the Pd_3Si network still solidified first before the dendritic growth of Pd_5Si.

The origin of solidification in Fig. 4 is further examined by SEM, as shown in Fig. 5. The width of the branches of the Pd_3Si network is about 0.6 μm, which is the finest dimensions of the Pd_3Si network in the specimen. This area of finest network is isotropic and it covers about 100 μm x 100 μm. Beyond this isotropic area, the Pd_3Si network gradually aligns radially, as shown in Fig. 6. The alignment causes elongation, necking and clustering of the branches of the network. This radial alignment gradually disappears and ends up finally with a coarsened (~ 2 μm) isotropic network of Pd_3Si as shown in Fig. 7. Comparing Fig. 5 and Fig. 7, the network in the starting area of solidification is finest and well-connected while the network some distance away is coarsened, rounding off and nearly broken.

The specimen that crystallized just below the spinodal curve (ΔT = 220 K) shows a somewhat different morphology. In the specimen that crystallized at ΔT = 230 K, there is only a small region of fine spinodal structure. This region covers an area of roughly 500 μm x 500 μm and the microstructure is similar to Fig. 4: a coarse, radial structure of Pd_5Si dendrites superposed by a fine, radially aligned Pd_3Si network (the network is also isotropic in the central portion). Beyond this region, the

fine network of Pd_3Si gradually breaks up (Fig. 8), coarsens and finally grows into large dendrites of Pd_3Si, as shown in Fig. 9.

We have also prepared specimens which were cooled in air after fluxing and crystallized in the spinodal region. The cooling rate was ~20 K/s, about two orders faster than the above method. The duration of crystallization was observed to be about 0.1 s. The microstructure of an as prepared specimen that crystallized at $\Delta T = 280$ K is shown in Fig. 10. When comparing Fig. 1 and Fig. 10, which correspond to two specimens both solidified at $\Delta T = 280$ K but with different cooling rates, the major difference is that the Pd_3Si network of the air-cooled specimen is better connected and less rounded off. The dimensions of the Pd_3Si network of the air-cooled specimen is about 0.8 μm. The overall morphology of the spinodal network of the air-cooled specimens looks more homogeneous, isotropic and has better connectivity.

Discussion

Summarizing our observations, we propose the crystallization process as follows, in view of the liquid miscibility gap in Fig. 13 of chapter two.

When a purified melt of $Pd_{80}Si_{20}$ is cooled down at 10 K/min, it will be undercooled below the solidus and reach the liquid miscibility gap at $\Delta T = 190$ K. If the melt has been sufficiently purified, it can bypass the region of liquid phase separation by nucleation and growth without being phase separated. Therefore, it is still homogeneous on reaching the liquid spinodal region at $\Delta T = 220$ K. At $\Delta T = 220$ K and below, it undergoes spinodal decomposition, resulting in two

networks of undercooled liquid phases. The composition of one of the two liquid phases is close to the composition of Pd_3Si (called liquid network A in the followings) and the other is close to the composition of Pd_5Si (called liquid network B) according to the liquid miscibility gap proposed (Fig. 13 in chapter two). Then, on further undercooling, the composition of the liquid network A will shift more and more close to that of Pd_3Si. Since the melting point of Pd_3Si is 1343 K, the liquid network A is in fact much more undercooled than the liquid network B. Therefore, the liquid network A will suddenly crystallize first while the liquid network B is still in an undercooled liquid state.

In the region where solidification starts, the liquid network A, with its composition close to but not exactly equal to Pd_3Si, crystallizes to form an isotropic Pd_3Si network and small Pd crystallites are precipitated out to the edge of or inside the Pd_3Si network (Fig. 5). The original morphology of the liquid network A is therefore frozen on solidification in this region. When the solidification interface of the liquid network A advances radially outward, the volume contraction on crystallization will pull the liquid network A in front of the interface, causing radial alignment and elongation of the branches of the liquid network A. Meanwhile, the latent heat released due to crystallization raises the temperature of the whole specimen and hence the wavelength of the liquid spinodal increases gradually from ~ 0.6 μm at the starting point of solidification to ~ 2 μm at far away. The rise in temperature also causes gradual coarsening, rounding off and necking of the liquid network away from the initial solidification center. Then, the arrival of the solidification front of the Pd_3Si

network freezes all these distorted morphologies of the liquid network A (Fig. 6 and Fig. 7).

As the crystallization goes on in the liquid network A, the liquid network B is still an undercooled liquid. Then the precipitation of Pd at the edges of the Pd_3Si network from B drives the composition of B to Pd_5Si. At the initial crystallization site of Pd_3Si, it is expected that the remaining undercooled liquid B reaches a composition of Pd_5Si first and starts the crystallization of B. It then grows out dendritically (Fig. 4). The polycrystallinity of Pd_5Si grains can be well explained by the abundance of numerous Pd seeds precipitated during the crystallization of the Pd_3Si network.

The specimen that crystallized at $\Delta T = 230$ K, just below the spinodal curve, clearly shows the effect of temperature inversion on a spinodal liquid. When the specimen was undercooled more than 220 K and then crystallized at $\Delta T = 230$ K, the fine structure of the spinodal decomposed liquid was frozen on solidification only in a small region around the starting area of crystallization. Then, the latent heat released raised the temperature of the specimen above the liquid miscibility gap. Hence the remaining spinodal liquid transformed back to a homogeneous liquid before the arrival of the solidification front. Since the homogenized liquid was still at an undercooled temperature, the solidifying branches of the Pd_3Si network then became dendritically growing into the remaining undercooled liquid, forming large dendrites of Pd_3Si (Fig. 9).

Finally, the morphology of the air-quenched specimen can be understood in terms of the fast crystallization rate. As the crystallization rate of the air-quenched

specimen was observed to be a few times faster than that of the slowly cooled specimens, there would be much less time for any rearrangement or distortion of the liquid spinodal network. Hence, the homogenity, isotropy and connectivity of the original liquid spinodal structure were much better preserved in the crystalline state of the air-quenched specimen (Fig. 10).

In conclusion, a metastable spinodal decomposed melt of $Pd_{80}Si_{20}$ crystallizes to form a fine interconnected structure of crystalline Pd_3Si and Pd_5Si. The crystallization of Pd_3Si sub-network always precedes and triggers the crystallization of Pd_5Si sub-network. After solidification, the original isotropic spinodal structure of the melt is basically preserved in the crystalline state but partially distorted by the aligning effect due to volume contraction and the coarsening effect due to latent heat released during crystallization.

References

1. **Chapter two of this thesis.**
2. **Chapter three of this thesis.**
3. **J.L. Walker, in 'B. Chalmers (Ed.): Principle of Solidification', p. 114 and 122 (Wiley 1964).**

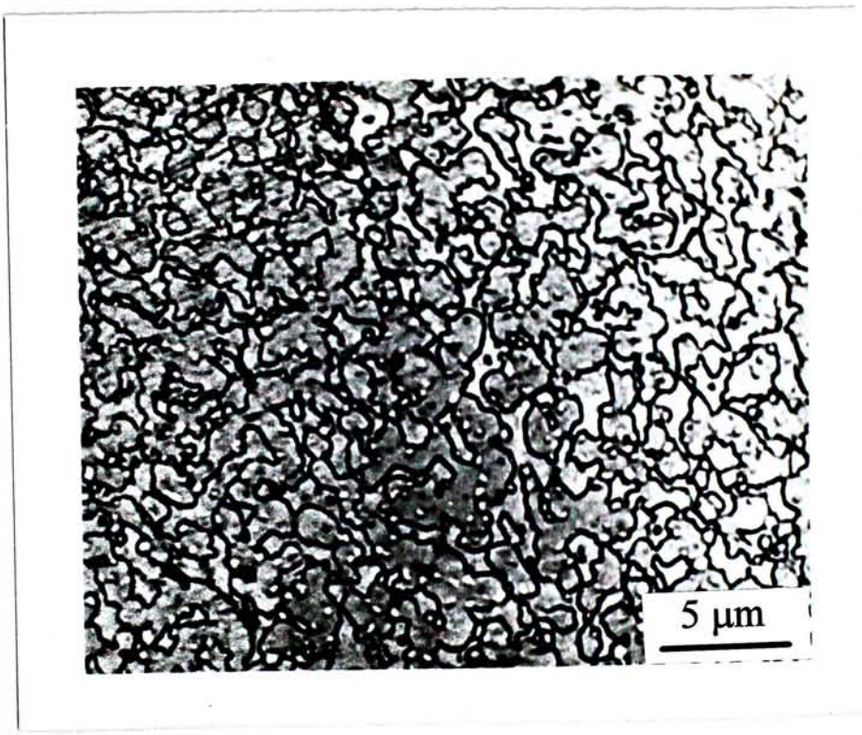

Fig. 1 Microstructure of a specimen of $Pd_{80}Si_{20}$ that crystallized at an undercooled temperature $\Delta T = 280$ K.

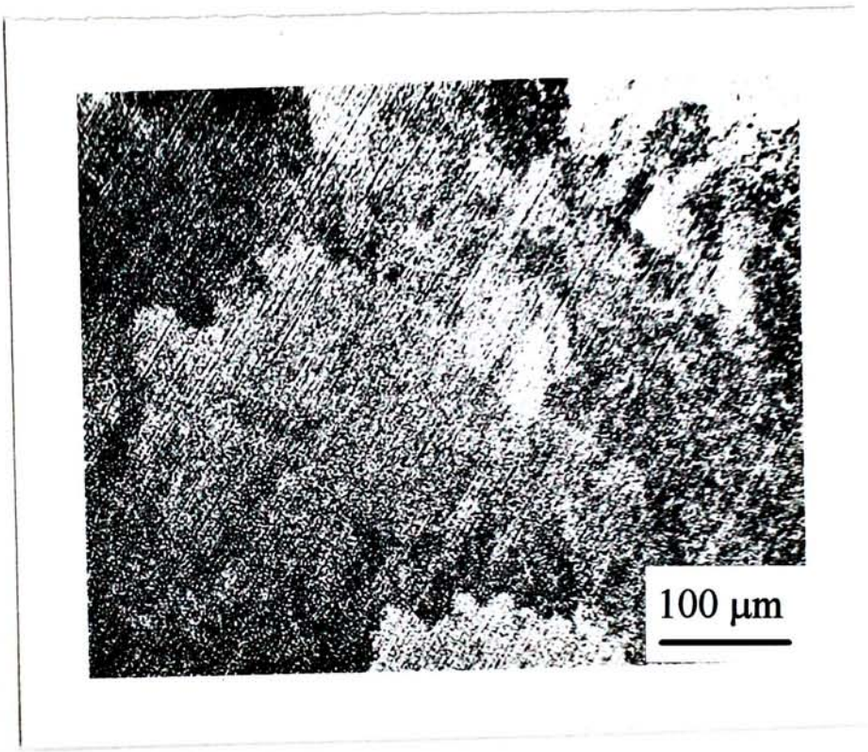

Fig. 2 Pd_5Si grains in the same specimen as shown in Fig. 1, superposed by a fine network of Pd_3Si.

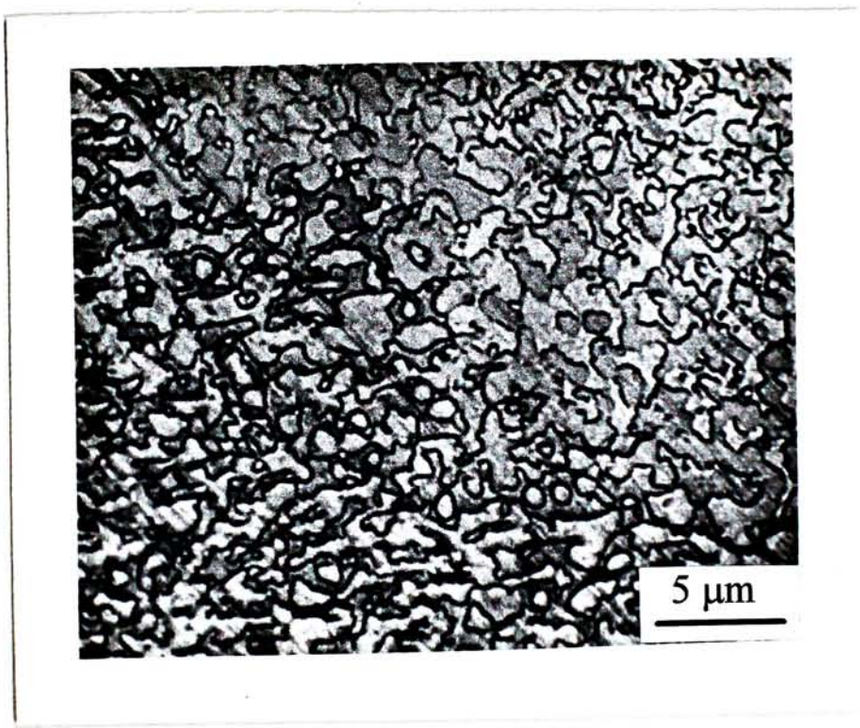

Fig. 3 Grain boundary of Pd_5Si superposed by the Pd_3Si network. The darker and lighter region correspond to two different Pd_5Si grains.

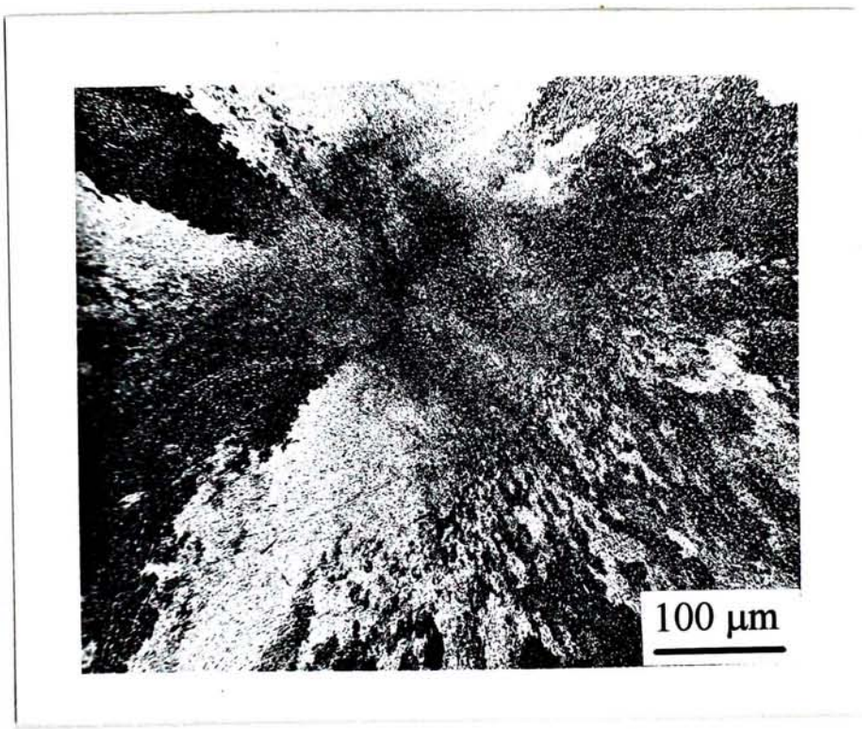

Fig. 4 Pd_5Si dendrites growing out from the solidification center. (The dendrites are also superposed by a fine network of Pd_3Si)

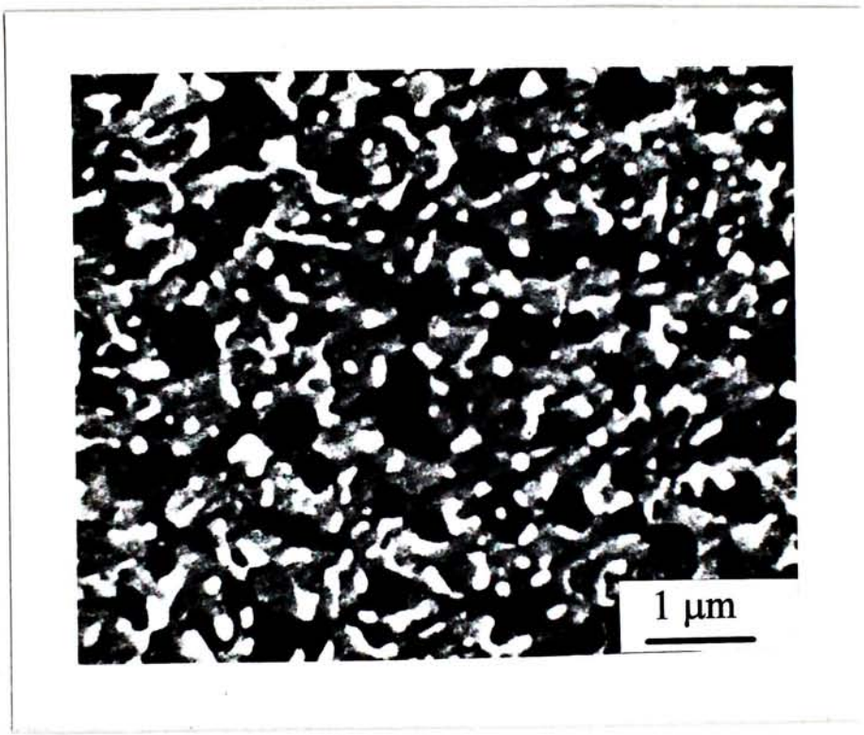

Fig. 5 SEM micrograph of the solidification center in Fig. 4.

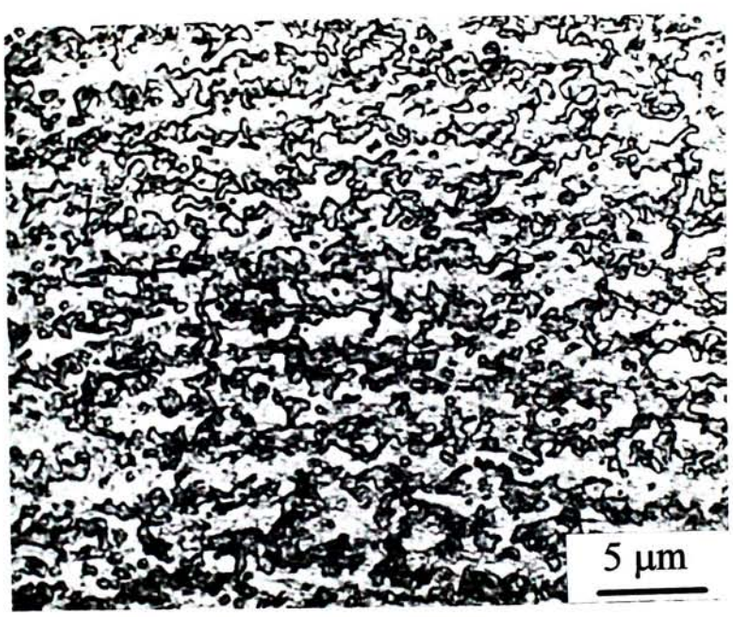

Fig. 6 Alignment of the Pd_3Si network beyond the solidification center in Fig. 4.

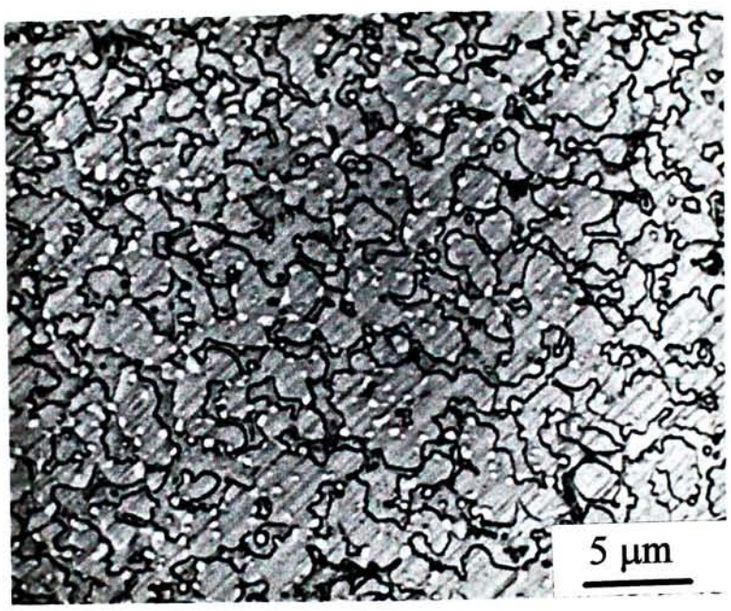

Fig. 7 Coarsened Pd_3Si network at far away from the solidification center in Fig. 4.

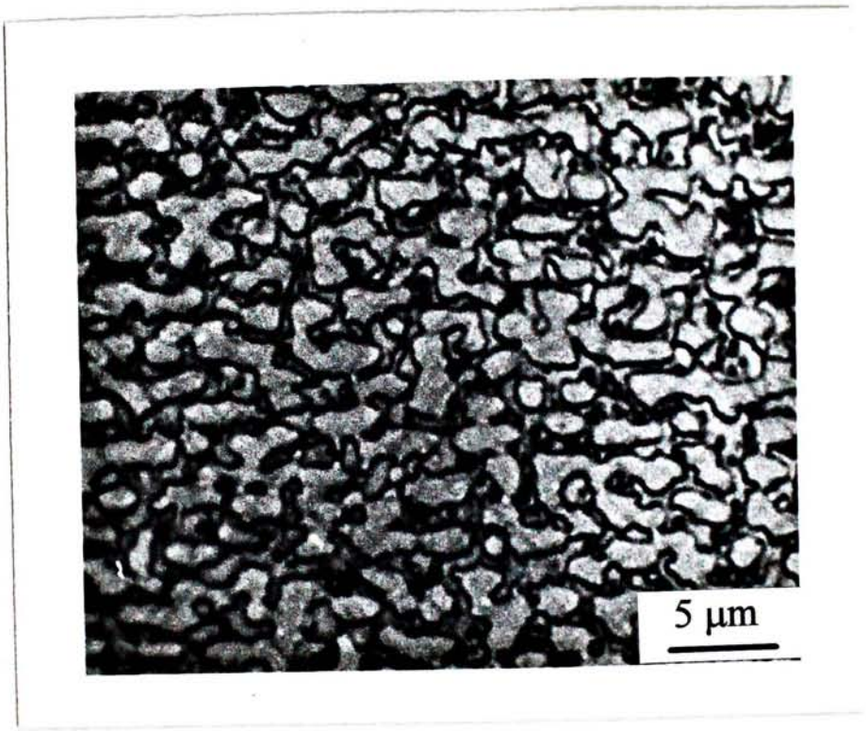

Fig. 8 Breaking of the Pd_3Si network in the specimen crystallized at $\Delta T = 230$ K.

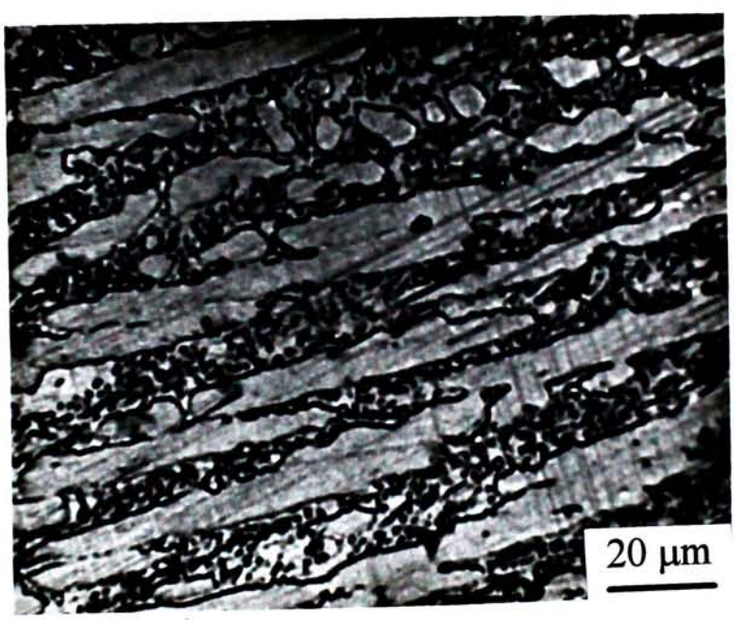

Fig. 9 Large dendrites in the specimen crystallized at $\Delta T = 230$ K.

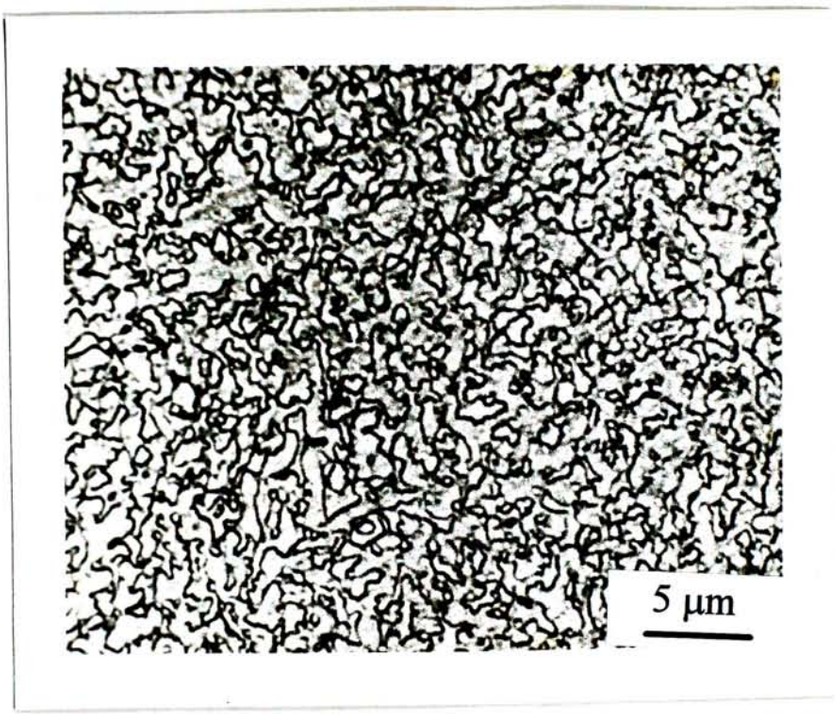

Fig. 10 Microstructure of the air-cooled specimen crystallized at $\Delta T = 280$ K.